A&A 542, A115 (2012)
DOI: 10.1051/0004-6361/201118379

Astronomy & Astrophysics

Crossing the Gould Belt in the Orion vicinity⋆,⋆⋆

K. Biazzo[1], J. M. Alcalá[1], E. Covino[1], M. F. Sterzik[2], P. Guillout[3], C. Chavarría-K.[4], A. Frasca[5], and R. Raddi[6]

[1] INAF – Osservatorio Astronomico di Capodimonte, via Moiariello, 16, 80131 Napoli, Italy
e-mail: katia.biazzo@oacn.inaf.it
[2] ESO – European Southern Observatory, Casilla 19001, Santiago 19, Chile
[3] Observatoire Astronomique de Strasbourg, CNRS, UMR 7550, 11 rue de l'Université, 67000 Strasbourg, France
[4] Instituto de Astronomía, Universidad Nacional Autónoma de Mexico, Ensenada, B. C., 22800, Mexico
[5] INAF – Osservatorio Astrofisico di Catania, via S. Sofia, 78, 95123 Catania, Italy
[6] Centre for Astrophysics Research, STRI, University of Hertfordshire, College Lane, Hatfield AL10 9AB, UK

Received 2 November 2011 / Accepted 16 April 2012

ABSTRACT

Context. The recent star formation history in the solar vicinity is not yet well constrained, and the real nature of the so-called Gould Belt is still unclear.
Aims. We present a study of the large-scale spatial distribution of 6482 ROSAT All-Sky Survey (RASS) X-ray sources in approximately 5000 deg^2 in the general direction of Orion. We examine the astrophysical properties of a sub-sample of ∼100 optical counterparts, using optical spectroscopy. This sub-sample is then used to investigate the space density of the RASS young star candidates by comparing X-ray number counts with Galactic model predictions.
Methods. The young star candidates were selected from the RASS using X-ray criteria. We characterize the observed sub-sample in terms of spectral type, lithium content, radial and rotational velocities, and iron abundance. A population synthesis model is then applied to analyze the stellar content of the RASS in the studied area.
Results. We find that stars associated with the Orion star-forming region, as expected, do show a high lithium content. As in previous RASS studies, a population of late-type stars with lithium equivalent widths larger than that of the Pleiades stars of the same spectral type (hence younger than ∼70−100 Myr) is found widely spread over the studied area. Two new young stellar aggregates, namely "X-ray Clump 0534+22" (age ∼ 2−10 Myr) and "X-ray Clump 0430−08" (age ∼ 2−20 Myr), are also identified.
Conclusions. The spectroscopic follow-up and comparison with Galactic model predictions reveal that the X-ray selected stellar population in the general direction of Orion is characterized by three distinct components, namely the clustered, the young dispersed, and the widespread field populations. The clustered population is mainly associated with regions of recent or ongoing star formation and correlates spatially with molecular clouds. The dispersed young population follows a broad lane that apparently coincides spatially with the Gould Belt, while the widespread population consists primarily of active field stars older than 100 Myr. We expect the still "bi-dimensional" picture emerging from this study to grow in depth as soon as the distance and the kinematics of the studied sources will become available from the future *Gaia* mission.

Key words. stars: late-type – stars: fundamental parameters – stars: individual: Gould Belt – techniques: miscellaneous – surveys – stars: individual: Orion

1. Introduction

If the global scenario of the star formation history (SFH) of the Milky Way is still not fully outlined (see Wyse 2009, for a review), the recent SFH in the solar neighborhood is far from being constrained. In particular, the recent local star formation rate is poorly known because of the difficulty encountered in properly selecting young late-type stars in large sky areas from optical data alone (Guillout et al. 2009). This situation has improved thanks to wide-field X-ray observations, such as the ROSAT[1] All-Sky Survey (RASS), which allowed for efficiently detecting of young, coronally active stars in the solar vicinity (Guillout et al. 1999). Nearby star-forming regions (SFRs) have been searched for pre-main sequence (PMS) stars, and many new nearby moving groups and widely-spread young low-mass stars have been identified over the past decades based on the RASS data (Feigelson & Montmerle 1999; Zuckerman & Song 2004; Torres et al. 2008; Guillout et al. 2009, and references therein).

It has been suggested that at least some of these widely spread young stars might be associated with the so-called Gould Belt (GB; Guillout et al. 1998), a disk-like structure made up of gas, young stars, and OB associations (see, e.g., Lindblad 2000; Elias et al. 2009). However, the existence of this structure and its possible origin remain somewhat controversial (Sánchez et al. 2007, and references therein). It is also unclear whether its putative young stellar population exceeds the predictions of Galactic models, which would indicate a recent episode of star formation. On the other hand, there is no evidence of molecular material within ∼100 pc that can explain the origin of the distributed young stars as in situ star formation. These young stars may therefore represent a secondary star formation event in clouds that condensed from the ancient Lindblad ring supershell,

⋆ Based on ROSAT All-Sky Survey data, low-resolution spectroscopic observations performed at the European Southern Observatory (Chile; Program 05.E-0566) and at the *Observatorio Astronómico Nacional de San Pedro Mártir* (Mexico), and high-resolution spectroscopic observations carried out at the Calar Alto Astronomical Observatory (Spain).

⋆⋆ Table 4 and Appendix A are only available in electronic form at http://www.aanda.org

[1] The RÖentgenSATellit is an X-ray observatory that operated for nine years since 1 June 1990, surveying the whole sky.

or may have been formed in recent bursts of star formation from already disrupted and evaporated small clouds (see Bally 2008, and references therein).

An accurate census of the young population in different star-forming environments and the comparison between observations and predictions from Galactic models are therefore required to constrain the low-mass star formation in the solar vicinity.

In this work, we revisit the results by Walter et al. (2000) on the large-scale spatial distribution of 6482 RASS X-ray sources in a 5000 deg^2 field centered on the Orion SFR, and use optical, low- and high-resolution spectroscopic observations to investigate the optical counterparts to 90 RASS sources (listed in Table 4) distributed on a sky "strip" perpendicular to the Galactic plane, in the general direction of Orion. The complete sky coverage of the RASS allows us to perform an unbiased analysis of the spatial distribution of X-ray active stars. Our main goal is to characterize spectroscopically the optical counterparts of the X-ray sources and compare their space density with predictions of Galactic models.

In Sect. 2 we define the sky areas and describe the selection of young X-ray emitting star candidates; in Sect. 3 we present the spectroscopic observations; in Sect. 4 we characterize the young optical counterparts in terms of spectral type, lithium detection, Hα line, radial/rotational velocity, and iron abundance; in Sect. 5 we compare the spatial distribution of the young X-ray emitting star candidates with expectations from Galactic models; in Sect. 6 we discuss the results and draw our conclusions.

2. Selection of study areas and X-ray sources

Our analysis is based on the method introduced by Sterzik et al. (1995) for selecting young star candidates from the RASS sources using the X-ray hardness ratios and the ratio of X-ray to optical flux. Figure A.1 is a revisited version of Fig. 3 by Walter et al. (2000), showing the color-coded space density of the RASS sources based on the α parameter, which is related to the probability of a source to be a young X-ray emitting star. Following the Sterzik et al. (1995) selection criteria, X-ray sources with $\alpha > 0.6$ are most likely young stars with a positive rate of 80%. In the figure we recognize i) the surface density enhancements corresponding to 1483 young candidates, distributed over an area much larger than the molecular gas; ii) space density enhancements not necessarily associated with previously known regions of active (or recent) star formation (e.g., at $\alpha = 5^h34^m$, $\delta = +22°01'$ and at $\alpha = 4^h30^m$, $\delta = -08°$); the local enhancement at $\alpha = 5^h07^m$ and $\delta = -03°20'$ corresponds to the L1616 cometary cloud (Alcalá et al. 2004; Gandolfi et al. 2008); iii) a broad lane apparently connecting Orion and Taurus, which extends further southeastward; this wide and contiguous structure is not symmetric about the Galactic plane, but instead seems to follow the GB as drawn by Guillout et al. (1998); iv) the surface density of young star candidates drops to a background value of about 0.1 candidate star/deg^2 near $b_{II} = 0°$, or below that value at higher Galactic latitudes.

In order to study the global properties of the different populations close to the Orion SFR, we selected a $10° \times 75°$ strip (see Fig. A.1) perpendicular to the Galactic plane (hence presumably crossing the GB), and in the Orion vicinity. Inside this ~750 deg^2 strip ($l_{II}^{min} = 195°$, $l_{II}^{max} = 205°$, $b_{II}^{min} = -60°$, $b_{II}^{max} = 15°$), 806 RASS X-ray sources were detected with a high-confidence level by the Standard Analysis Software System (SASS; Voges 1992). According to the Sterzik et al. (1995) selection criteria, 198 of these sources are young star candidates.

Table 1. Summary of the spectroscopic observations.

Telescope	Instrument	Range (Å)	Resolution ($\lambda/\Delta\lambda$)	# stars
1.5 m@ESO	B&Ch	3400–6800	1 600	66
2.1 m@OAN-SPM	B&Ch	3600–9900	1 500	6
2.2 m@CAHA	FOCES	4200–7000	30 000	61

Notes. 29 stars were observed only at low resolution, and 19 only at high resolution. One star was observed at low resolution with both the B&Ch spectrographs.

Additionally, we selected a region of $10°\times10°$ (see Fig. A.1) centered at $\alpha = 5^h34^m$ and $\delta = +22°01'$, where a density enhancement of young star candidates is present. We call this previously unrecognized enhancement "X-ray Clump 0534+22" (hereafter, X-Clump 0534+22). Analogously, we also identify as "X-ray Clump 0430−08" (hereafter, X-Clump 0430−08) the unknown density enhancement at $\alpha = 4^h30^m$ and $\delta = -08°$. Although X-Clump 0534+22 almost coincides in direction with the Crab nebula, it is physically unrelated to the supernova remnant.

3. Spectroscopic observations and data reduction

We conducted a spectroscopic follow-up of 90 young stellar candidates inside the strip and clump regions. Table 1 gives a summary of the spectroscopic observations, while the full list of the observed stars is reported in Table 4. Throughout the paper, we call "young star" an optical counterpart that shows characteristics typical of weak-lined T-Tauri stars, i.e. weak Hα emission ($EW_{H\alpha} \lesssim 10$ Å) and strong lithium absorption.

3.1. Low-resolution spectroscopy

Low-resolution spectroscopic observations were carried out during 25–30 November 1995 and 16–21 December 1996 using the Boller & Chivens (B&Ch) Cassegrain spectrographs attached to the 1.5 m telescope of the European Southern Observatory (ESO, Chile) and to the 2.1 m of the *Observatorio Astronómico Nacional de San Pedro Mártir* (OAN-SPM, Mexico), respectively. Table 1 gives information on the instrumental setups and number of observed objects. The spectral resolution was verified by measuring the full-width-at-half maximum of several lines in calibration spectra. The spectra were reduced following the standard procedure of MIDAS[2] software packages using the procedure described in Alcalá et al. (1996).

About sixty of the 198 strip sources plus fourteen stars in the X-Clump 0534+22 direction were investigated spectroscopically at low resolution (see Table 4 and Fig. 1). The observational strategy consisted in covering the whole range of right ascension and declination each night to avoid any bias in the resulting spatial distribution of the young star candidates. The spatially unbiased sample so far observed and characterized spectroscopically by us is therefore incomplete, representing ~40% of the total sample of potential young X-ray emitting candidates. Yet it can be used to study the strength of the lithium absorption line within the RASS young stellar sample as a function of Galactic latitude, and to trace the young stellar population in the general direction of Orion.

[2] The MIDAS (Munich Image Data Analysis System) system provides general tools for image processing and data reduction. It is developed and maintained by the ESO.

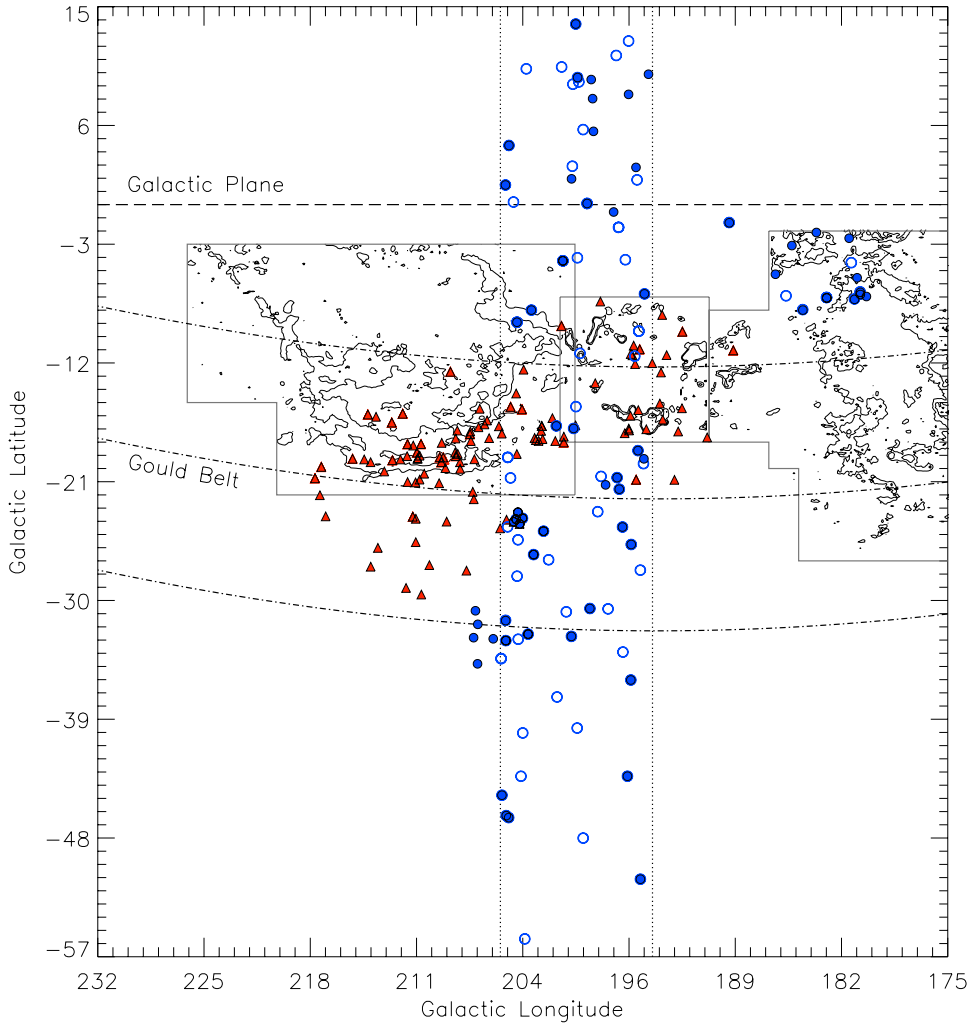

Fig. 1. Large-scale spatial distribution of our targets (circles) and those of Alcalá et al. (1996, 2000; triangles). Empty symbols refer to low-resolution spectra, while filled symbols represent objects observed at high resolution. The dotted lines mark the strip, the long-dashed line is the Galactic plane, while the dash-dotted lines represent the Gould Belt disk, as outlined by Guillout et al. (1998). The CO $J = 1 \rightarrow 0$ emission contour maps by Dame et al. (2001) of the Orion, Monoceros, and Taurus molecular clouds, and the λ Orionis H II region are also overlaid.

3.2. High-resolution spectroscopy

High-resolution spectroscopic observations were conducted in several runs in the period between October 1996 and December 1998, using the Fiber Optics Cassegrain Échelle Spectrograph (FOCES) attached to the 2.2 m telescope at the Calar Alto Observatory (CAHA, Spain). Some seventy spectral orders are included in these spectra, covering the range from 4200 to 7000 Å, with a nominal mean resolving power of $\lambda/\Delta\lambda \approx 30\,000$ (see Table 1). The reduction was performed using IDL[3] routines specifically developed for this instrument (Pfeiffer et al. 1998). Details on the data reduction are given in Alcalá et al. (2000).

We also retrieved FEROS[4] spectra for two stars of our sample (namely, 2MASS J03494386−1353108 and 2MASS J04354055−1017293) from the ESO Science Archive[5]. The FEROS spectra extend between 3600 Å and 9200 Å with a resolving power $R = 48\,000$ (Kaufer et al. 1999). The data were reduced using a modified version of the FEROS-DRS pipeline (running under the ESO-MIDAS context FEROS), which yields a wavelength-calibrated, merged, normalized spectrum, following the steps specified in Desidera et al. (2001).

In summary, high-resolution spectroscopy exists for 61 stars, 33 inside the strip, 13 in the X-Clump 0534+22, 8 associated with the high space-density X-Clump 0430−08 (see in Fig. A.1 the spatial distribution at $\alpha = 4^{\rm h}30^{\rm m}$ and $\delta = -08°$), and 7 inside the strip associated to the L1616 clump. The high-resolution sample thus represents ∼70% of the known lithium stars in the strip, and can be used to verify the reliability of the lithium strength obtained from the low-resolution spectra.

In order to increase the statistics, we also included in our analysis the on-strip lithium-rich stars identified by Alcalá et al. (1996) and Alcalá et al. (2000), which were observed with the same instruments, set-ups, and observational strategy.

4. Characterization of the selected young X-ray counterparts

4.1. Near-IR color–color diagram

We identified all our targets in the Two Micron Sky Survey (2MASS) catalog. In Table 4 we list the RASS Bright Source

[3] IDL (Interactive Data Language) is a registered trademark of ITT Visual Information Solutions.

[4] This is the Fiber-fed Extended Range Optical Spectrograph operating in La Silla (ESO, Chile) for the 1.5 m telescope.

[5] http://archive.eso.org/cms/

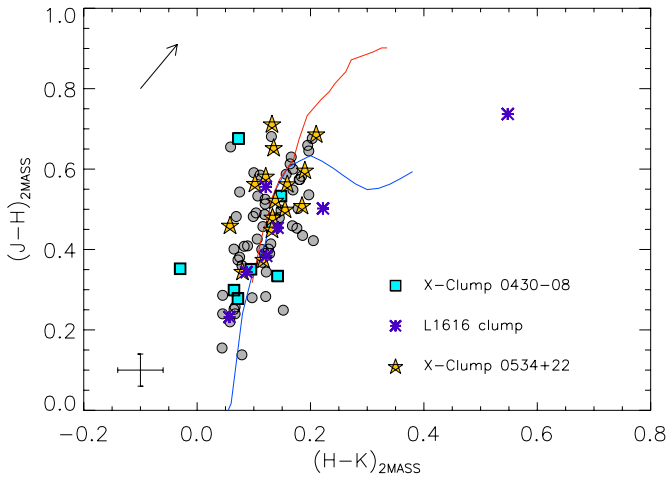

Fig. 2. 2MASS $(J-H)$ versus $(H-K)$ diagram for the observed sources. Squares, asterisks, and stars represent objects in the three clumps, as indicated in the legend. The circles refer to the "non-clump" stars. The solid curve shows the relation between these indexes for main sequence stars (lower branch; Bessell & Brett 1988) and giants (upper branch; Kenyon & Hartmann 1995), where the 2MASS color trasformations were used. The $A_V = 1$ mag reddening vector is shown with an arrow. The typical 2MASS photometric errors are overplotted on the lower-left corner of the panel.

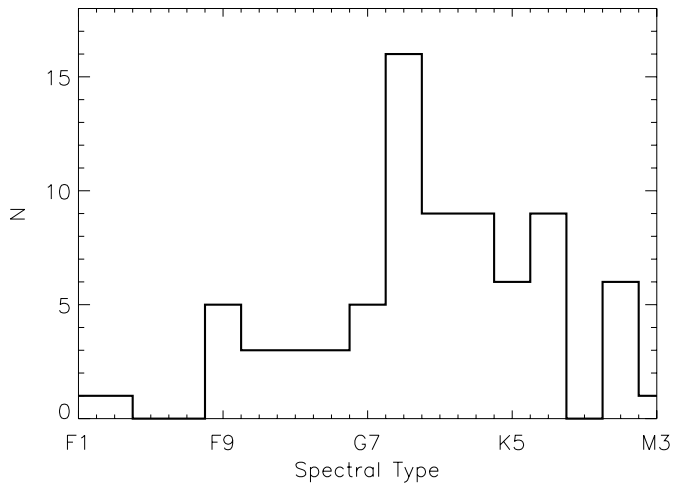

Fig. 3. Spectral type distribution of the young stellar candidates.

Catalog (Voges et al. 1999) and 2MASS designations, and an alternative name. The stellar coordinates are those from the 2MASS catalog. We then examined the properties of the sources in the JHK bands using their 2MASS magnitudes (Cutri et al. 2003) looking for possible color excess. The $(J-H)$ versus $(H-K)$ diagram (Fig. 2) shows that our sample mostly consists of stars without near-IR excess, with the only exception of 2MASS J05122053−0255523 = V531 Ori, which was classified as a classical T Tauri star by Gandolfi et al. (2008). All stars follow the MS branch with a spread mostly ascribable to photometric uncertainties. Only 2MASS J04405981−0840023 departs from the sequence, maybe because of its double-lined binary nature (Covino et al. 2001).

4.2. Spectral types, lithium detection, and Hα equivalent width

Spectral types were determined from the low-resolution spectra by comparison with a grid of bright spectral standard stars (from F0 to M 5) observed with the same dispersion and instrumental set-up in each observing run. The methods described in Alcalá et al. (1995) were used for the classification, leading to an accuracy of about ±1 sub-class in most cases. The spectral types are reported in Table 4, while their distribution is plotted in Fig. 3. The sample is composed of late-type stars with a distribution peaked around G9–K1.

In our low-resolution spectroscopic follow-up, the Orion stars fall basically into four categories (see Table 4): i) stars with weak Hα emission (-3 Å $\lesssim EW_{\mathrm{H}\alpha} \lesssim 0$ Å) and Li absorption (18 stars); ii) stars with Hα filled-in or in absorption and Li absorption (42 stars); iii) stars with Hα in emission but no Li absorption (eight stars); and iv) stars with Hα in absorption but no Li detection (four stars). In total, 60 stars with clear lithium detections were found throughout the strip and in the clumps. Practically all lithium stars have spectral types ranging from late F to K7/M0 peaking around G9 (see Table 4). The effective temperature versus spectral type relation for dwarfs by Kenyon & Hartmann (1995) was used to estimate the $\log T_{\mathrm{eff}}$ values listed in Table 4.

At this point, it is important to stress that i) at the Orion distance, our sample is limited to masses >0.8 $M_\odot$ (Alcalá et al. 1998) because of the RASS flux limit; ii) the Li equivalent width (EW_{Li}) may be overestimated in low-resolution spectra because of blending mainly with the nearby Fe I line at $\lambda = 6707.4$ Å (see Sect. 4.3). This problem can be overcome by using high-resolution spectroscopy (see Sects. 3.2 and 4.3).

4.3. Lithium strength: low-versus high-resolution measurements

For 43 stars we obtained both low- and high-resolution spectra. Based on these data, we estimated that the mean lithium equivalent width measured on low-resolution spectra ($EW^{\mathrm{lr}}_{\mathrm{Li}}$) is overestimated by ∼20 mÅ, with a standard deviation of ±60 mÅ on the average difference between the low- and high-resolution measurements. Interestingly, for several stars, the $EW^{\mathrm{lr}}_{\mathrm{Li}}$ matches the lithium equivalent width obtained from high-resolution spectra ($EW^{\mathrm{hr}}_{\mathrm{Li}}$) well and, in some cases, $EW^{\mathrm{lr}}_{\mathrm{Li}}$ values are underestimated (see Table 4). The good match between the $EW^{\mathrm{lr}}_{\mathrm{Li}}$ and $EW^{\mathrm{hr}}_{\mathrm{Li}}$ values can be attributed to the lithium strength of these stars, which is indeed high and also to the experience we gathered on measuring EW_{Li} in low-resolution spectra.

In Fig. 4 (left panel), the lithium equivalent widths of the 47 stars in our sample and the 38 from Alcalá et al. (1996), observed at low-resolution and falling inside the strip, are plotted versus the logarithm of the effective temperature, for the following three bins of Galactic latitude: i) $-20° < b_{\mathrm{II}} < -10°$, coinciding with the Orion complex; ii) $-30° < b_{\mathrm{II}} < -20°$, corresponding approximately to the position of the Gould Belt at those Galactic longitudes; and iii) in the two ranges $-10° < b_{\mathrm{II}} < 15°$ and $-60° < b_{\mathrm{II}} < -30°$ (directions that we consider as likely dominated by field stars). Similar plots were produced for the stars observed at high resolution (see right panel of Fig. 4). The upper envelope for the Pleiades stars, adapted from the Soderblom et al. (1993) data, is also overplotted. In both panels, a spatial segregation of lithium strength can be observed, which justifies using both high- and low-resolution EW_{Li}. Practically all stars in the Orion region are located above the Pleiades upper envelope, as expected. The majority of these stars are indeed

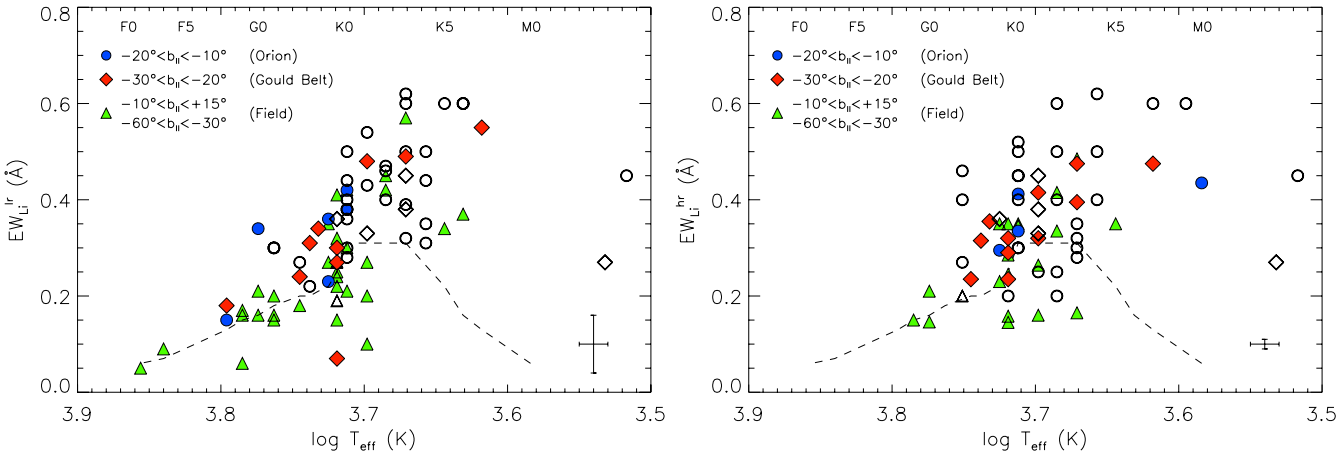

Fig. 4. Lithium (λ6707.8 Å) equivalent width versus $\log T_{\rm eff}$ for the stars in the strip ($195° < l_{\rm II} < 205°$), observed at low (*left panel*) and high (*right panel*) resolution. Three different bins of Galactic latitude were considered (see also Fig. 1). The upper envelope for the Pleiades sample, as adapted from Soderblom et al. (1993), is overplotted as a dashed line. Mean errors in $EW^{\rm lr}_{\rm Li}$ (~60 mÅ), $EW^{\rm hr}_{\rm Li}$ (~10 mÅ), and $\log T_{\rm eff}$ (~100 K, as obtained from the spectral synthesis) are overplotted on the lower-right corner of each panel. Open symbols represent the Alcalá et al. (1996) and Alcalá et al. (2000) results from low- (*left panel*) and high- (*right panel*) resolution spectra, respectively.

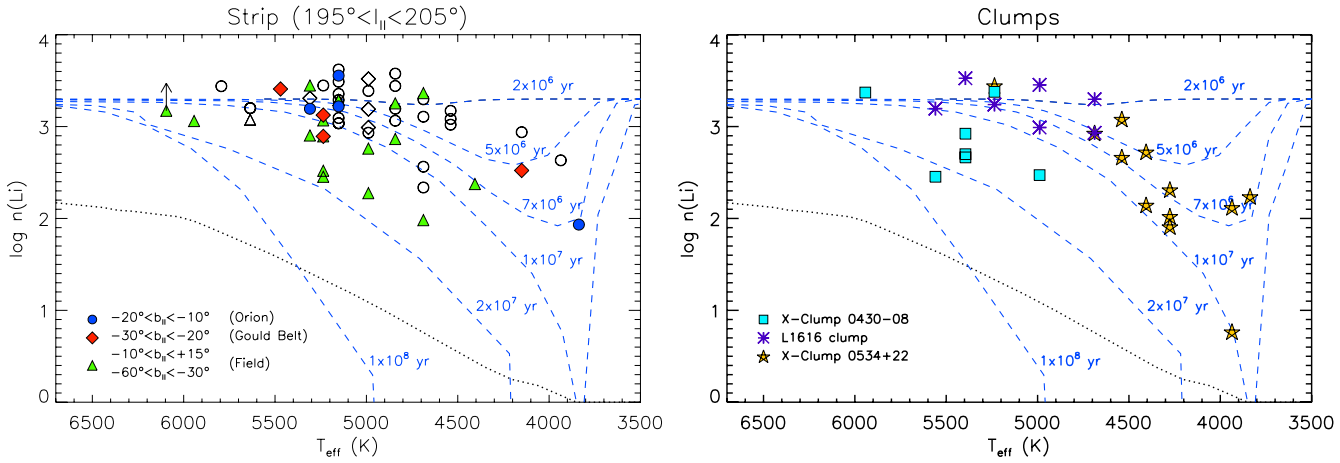

Fig. 5. Lithium abundance versus effective temperature for stars observed at high resolution (filled symbols refer to our sample, while open symbols represent the Alcalá et al. (2000) measurements). The "lithium isochrones" by D'Antona & Mazzitelli (1997) in the 2×10^6–1×10^8 yr range are overlaid with dashed lines. Dotted lines represent the limiting detectable $\log n$(Li), as derived from the Pavlenko & Magazzù (1996) non-LTE curves-of-growth, assuming 10 mÅ as mean $EW_{\rm Li}$ error and adding quadratically the mean contribution of the iron line at 6707.4 Å computed from the empirical relation obtained by Soderblom et al. (1993) between $B - V$ color and $EW_{\rm Fe}$ (Kenyon & Hartmann 1995, tables were used to convert $B - V$ colors into $T_{\rm eff}$). *Left panel*: stars located along the strip crossing the GB in the range $195° < l_{\rm II} < 205°$ (see Fig. 1) and three bins of Galactic latitude. *Right panel*: stars in known (L1616) and unknown (X-Clump 0430−08 and X-Clump 0534+22) groups.

very young. Note that many stars, located in the region of the hypothetical Gould Belt, also have strong lithium absorption but tend to be closer to the Pleiades upper envelope. Finally, the majority of the lithium field stars are located closer to/or below the Pleiades upper envelope, and most of them seem to have an age similar to the Pleiades or older. Nevertheless, a few of these field stars have lithium strengths comparable to those of stars in Orion or the Gould Belt direction, and seem to also be very young.

4.3.1. Lithium abundance

The lithium abundance ($\log n$(Li)) was derived from the $EW^{\rm hr}_{\rm Li}$ and $T_{\rm eff}$ values and using the non-LTE curves-of-growth reported by Pavlenko & Magazzù (1996), assuming $\log g = 4.5$. The main source of error in $\log n$(Li) is the uncertainty in $T_{\rm eff}$, which is about $\Delta T_{\rm eff} = 150$ K. Taking this value and a mean error of about 10 mÅ in $EW_{\rm Li}$ into account, we estimate a mean $\log n$(Li) error ranging from ~0.22 dex for cool stars ($T_{\rm eff} \approx 3700$ K) down to ~0.13 dex for warm stars ($T_{\rm eff} \approx 5800$ K). Moreover, the assumption of $\log g = 4.5$ affects the lithium abundance determination, in the sense that the lower the surface gravity, the higher the lithium abundance. In particular, the difference in $\log n$(Li) may rise to ~0.1 dex, when considering stars with mean values of $EW_{\rm Li} = 300$ mÅ and $T_{\rm eff} = 5000$ K and assuming $\Delta \log g = 1.0$ dex. Hence, this means that our assumption of $\log g = 4.5$ would eventually lead us to underestimate the lithium abundance.

In Fig. 5 (left panel), we show the lithium abundance as a function of the effective temperature for the stars on the strip, but coded in three bins of Galactic latitude, hence, according to their spatial location with respect to the Orion SFR and the Gould Belt. We also overplot the isochrones of lithium burning as calculated by D'Antona & Mazzitelli (1997). Three groups

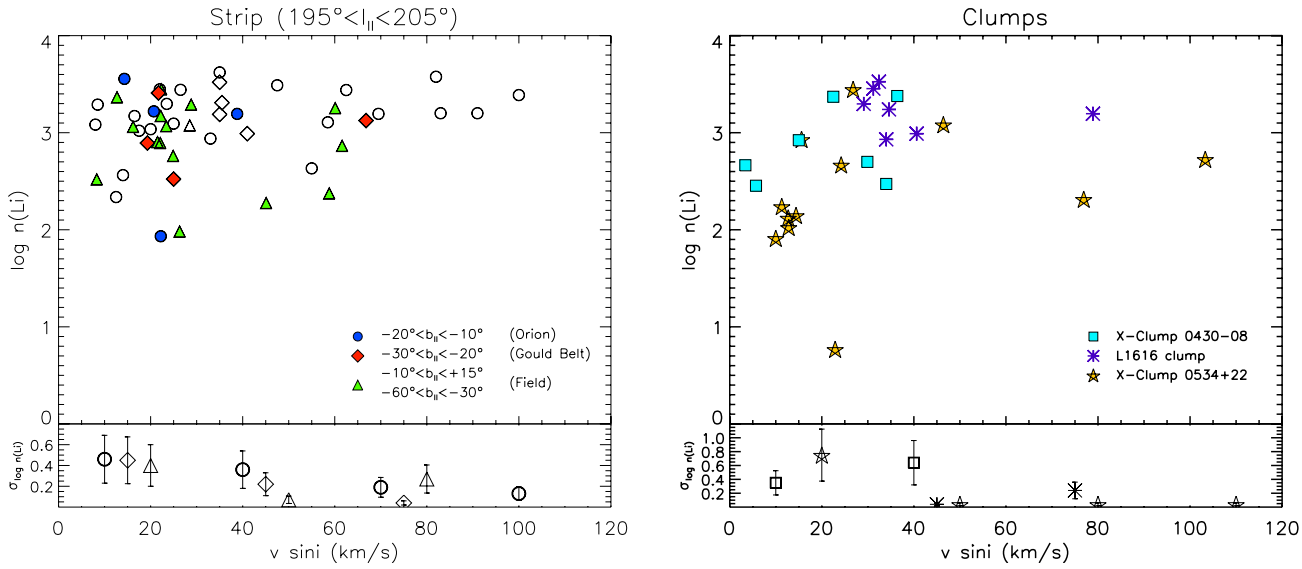

Fig. 6. Lithium abundance versus $v \sin i$ for stars observed at high resolution. Symbols as in Fig. 5. Bottom panels show for each group the $\log n$(Li) dispersion as a function of $v \sin i$ at the following bins: 0–30, 30–60, 60–90, 90–120 km s^{-1}. The values are shifted in $v \sin i$ to better visualize the symbols.

of stars can be identified according to the lithium content and spatial location. First, stars showing high-lithium content with ages even younger than $\sim 2-5 \times 10^6$ yr, mostly located on or close to the Orion clouds; second, stars with lithium content consistent with ages $\sim 5 \times 10^6 - 1 \times 10^7$ yr, supposedly distributed along the Gould Belt, and third, stars with lithium indicating a wide range of ages, but located far off the Orion SFR or the GB.

In Fig. 5 (right panel), we show the same plot, but for the three identified young aggregates, represented by three different symbols. The lithium content in the X-Clump 0430−08 corresponds to an age of about $2 \times 10^6 - 2 \times 10^7$ yr, while for the L1616 group it indicates an age of $2-7 \times 10^6$ yr, consistent with the Alcalá et al. (2004) and Gandolfi et al. (2008) findings. Finally, the lithium content of the stars in X-Clump 0534+22 indicates a relatively narrow age range of 2−10 Myr, which is consistent with the age inferred from the HR diagram when adopting a distance of 140 pc (see Sect. 5.2).

4.3.2. Rotational and radial velocity measurements

Stellar rotation may affect internal mixing, hence lithium depletion. A large spread in rotation rates may introduce a spread in lithium abundance, which is observed in young clusters (Balachandran et al. 2011, and references therein). To investigate this Li behavior in the stars of our sample, rotational ($v \sin i$) velocities were derived by using the same cross-correlation method as described in Alcalá et al. (2000).

In Fig. 6 (left panel) we show the lithium abundance versus $v \sin i$ for the on-strip stars, coded with three different symbols, indicating their spatial location as defined in the previous section. Despite the low statistics, the typical $\log n(\mathrm{Li}) - v \sin i$ behavior observed in young clusters, i.e. a larger spread in $\log n$(Li) for lower $v \sin i$ values, is apparent for the stars projected on Orion and the Gould Belt. To assign a confidence level to this trend, a one-side 2×2 Fisher's exact test[6] was performed (Agresti 1992). For the test, we adopted 30 km s^{-1} and 2.0 dex as dividing limits in $v \sin i$ and $\log n$(Li), respectively. We found a p-value of 0.54 as chance that random data would yield the trend, indicating a correlation probability of 46%. Hence, the low-number statistics prevents a rigorous demostration of the apparent trend shown in the plots. More measurements of $\log n$(Li) and $v \sin i$ for stars projected on Orion and the Gould Belt are needed to firmly establish the preservation of Li content at high $v \sin i$ ($\gtrsim$25 km s^{-1}) values. The above $\log n(\mathrm{Li}) - v \sin i$ behavior is even less evident, however, for the stars flagged as "field". These stars show a spread in $\log n$(Li) at all $v \sin i$ values. The difference between the three stellar groups is supported by the different dispersion in the $\log n(\mathrm{Li}) - v \sin i$ diagram (see left-bottom panel of Fig. 6).

In Fig. 6 (right panel) the lithium abundance is plotted as a function of $v \sin i$ for the stars in the young aggregates. Similar conclusions can be achieved as for the young stars projected on Orion and the Gould Belt. The $\log n(\mathrm{Li}) - v \sin i$ behavior in the X-Clump 0534+22 aggregate is enhanced by the star with the lowest lithium abundance and low $v \sin i$. This star, namely 2MASS J06020094+1955290, shows basically the same activity level as the other targets (see $EW_{\mathrm{H}\alpha}$ in Table 4 and $\log \frac{f_X}{f_V}$ values in the histograms of the top panel of Fig. 10) and is indistinguishable from the other stars in the aggregate.

Stellar radial velocities (RV) were also measured by means of cross-correlation analysis. In Fig. 7 (left panel) we show the distribution of RV for the on-strip stars, also divided into three bins of Galactic latitude as above. While the field stars show a wide RV range, the RV distribution of the stars projected on Orion and the GB is peaked at values of $\sim$18 km s^{-1}, i.e. close to the tail at low RV of the Orion sub-associations (from 19.7 ± 1.7 km s^{-1} for 25 Ori to 24.87 ± 2.74 km s^{-1} for the ONC, to $\sim 30.1 \pm 1.9$ km s^{-1} for OB1b; see, Briceño et al. 2007; Biazzo et al. 2009) or to the Taurus-Auriga distribution (16.03 ± 6.43 km s^{-1}; Bertout & Genova 2006).

In Fig. 7 (right panel) the RV distribution of the stars in the young aggregates is shown. With the exception of two stars in the X-Clump 0430−08, likely spectroscopic binaries, the RV of these groups is in the range 10–35 km s^{-1}, fairly consistent with Orion or Taurus. It is worth mentioning that the RV distribution of widely distributed young stars in Orion shows a double peak

[6] We used the following web calculator (Langsrud et al. 2007): http://www.langsrud.com/fisher.htm

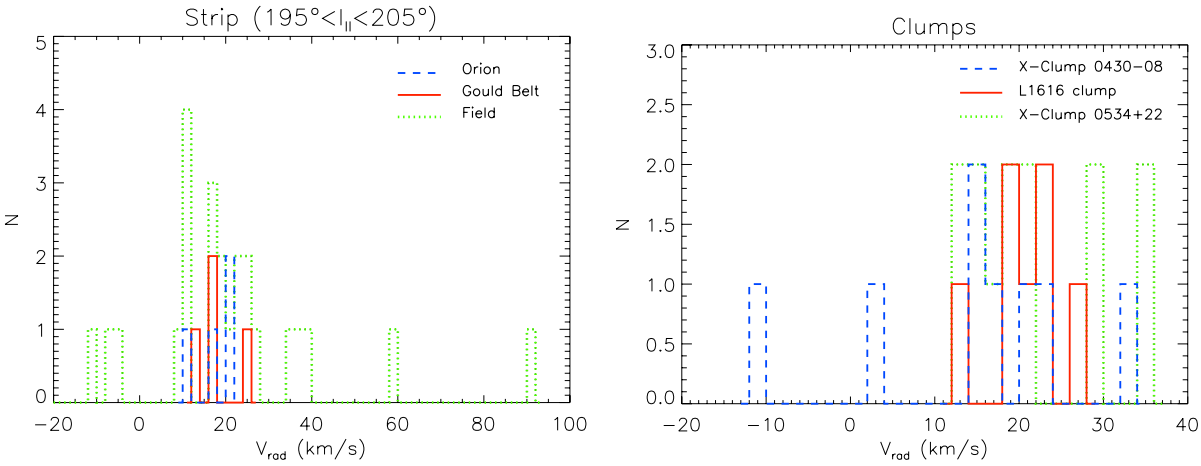

Fig. 7. Radial velocity distribution for the on-strip stars (*left panel*) and in the young aggregates (*right panel*), respectively.

(Alcalá et al. 2000), which can be explained as caused by objects associated with different kinematical groups, likely located at different distances.

4.3.3. Iron abundance

Metallicity measurements were obtained following the prescriptions by Biazzo et al. (2011a,b) and the 2010 version of the MOOG[7] code (Sneden 1973).

After screening the sample to select suitable stars (G0-K7 stars with $v \sin i \lesssim 20$ km s^{-1} and no evidence of multiplicity), a total of 11 stars in our sample, plus 8 stars from Alcalá et al. (2000) were analyzed for iron abundance measurements. In Table 2 we list the final results, together with effective temperature, surface gravity, and microturbulence (the number of lines used is also given in Cols. 6 and 8). An initial temperature value was set using the ARES[8] automatic code (Sousa et al. 2007, 2010); initial microturbulence was set to $\xi = 1.5$ km s^{-1}, and initial gravity to $\log g = 4.0$. The effective temperatures derived using this method and from spectral types (Sect. 4.2) agree within ~200 K (i.e. ~1.5 spectral sub-class) on average. For the stars observed with the FOCES and FEROS spectrographs, the values of the stellar parameters closely agree. It is worth noticing that the target 2MASS J05214684+2400444 was also analyzed by Santos et al. (2008; their 1RXS J052146.7), who derived stellar parameters ($T_{\rm eff} = 4921 \pm 59$ K, $\log g = 4.05 \pm 0.29$, $\xi = 1.92 \pm 0.07$ km s^{-1}, $v \sin i = 13$ km s^{-1}) and an iron abundance ([Fe/H] $= -0.07 \pm 0.07$) that agree well with our determinations, thus excluding any significant systematic error due to different datasets (see Biazzo et al. 2011b).

In Figs. 8 and A.2 we show the iron abundance distribution for the stars with strong lithium absorption (16 stars representing the young population) and those without it (three stars representing the old field population). Two results are noticeable: i) the stars with high lithium content show a distribution with a mean [Fe/H][9] $= -0.02 \pm 0.09$, consistent with the value of -0.01 ± 0.03 for open clusters younger than 150 Myr and within 500 pc from the Sun (see Biazzo et al. 2011a, for details); ii) stars with no lithium absorption line show [Fe/H] values that are within the metallicity distribution of field stars in the solar neighborhood ([Fe/H] $= -0.10 \pm 0.24$; Santos et al. 2008). This would imply that the young stars in the Orion vicinity have solar metallicity, consistent with the distribution of the Galactic thin disk in the solar neighborhood (Biazzo et al. 2011b).

[7] http://www.as.utexas.edu/~chris/moog.html
[8] http://www.astro.up.pt/~sousasag/ares/
[9] [Fe/H] $= \log n^{\star}$(Fe I/H) $- \log n^{\odot}$(Fe I/H)

5. Discussion

5.1. RASS and Galactic models

How many young, X-ray active stars are expected inside the strip? A comparison of the *number counts* with predictions from Galactic models provides the basis for a quantitative analysis of source excesses (or deficits) in order to understand their origin. Because of the strong dependence of stellar X-ray emission on age, an X-ray view of the sky preferentially reveals young stars (ages ≤100 Myr), in contrast to optical star counts, which only loosely constrain the stellar population for ages ≤10^9 yr. A Galactic X-ray star count modeling starts by adopting a Galactic model, including assumptions about the spatial and temporal evolution of the star formation rate and the initial mass function, and uses characteristic X-ray luminosity functions attributed to the different stellar populations. These models are able to predict the number of stars per square degree $N(>S)$ with X-ray flux $>S$, taking into account the dependence on Galactic latitude, spectral type, and stellar age. An elaborate Galactic model, including kinematics, is the *evolution synthesis population model* developed at Besançon (Robin & Crézé 1986), which computes the density and the distribution of stars as a function of the observing direction, age, spectral type, and distance. Our X-ray synthetic model is based on the Besançon optical model and has been first applied to the analysis of the RASS stellar population by Guillout et al. (1996). Motch et al. (1997) successfully used this model in a low Galactic latitude RASS area in Cygnus and found a good agreement between observations and predicted number counts using the "canonical" assumption of a uniform and continuous star formation history in the solar vicinity. We note, however, that following the publication of Hipparcos results, the stellar density in the solar neighborhood was revised (lowered) in the Besançon model, thus propagating model predictions in the X-ray population. The apparent disagreement between observed and predicted number count (by ~20%) can in fact be explained by the population of old close binaries (RS CVn-like systems), as suggested by Favata et al. (1988) and Sciortino et al. (1995). RS CVn systems for which the high magnetic activity level results from the synchronization of rotational and orbital periods can mimic young active stars and contam-

Table 2. Spectroscopic stellar parameters and iron abundance derived with MOOG for low-rotating stars observed at high resolution.

Star	$T_{\rm eff}$ (K)	$\log g$ (dex)	ξ (km s^{-1})	[Fe I/H]* (dex)	# Lines	[Fe II/H]** (dex)	# Lines
X-Clump 0534+22							
2MASS J05263833+2231546	4750	4.4	2.0	−0.08 ± 0.15	43	−0.08 ± 0.15	3
2MASS J05263826+2231434	4750	4.0	1.9	−0.07 ± 0.12	42	−0.06 ± 0.11	5
2MASS J05214684+2400444	5000	4.3	2.2	−0.04 ± 0.11	44	−0.02 ± 0.06	4
X-Clump 0430−08							
2MASS J04431640−0937052	6000	4.6	1.4	+0.22 ± 0.08	66	+0.22 ± 0.10	9
″	*6050*	*4.6*	*1.4*	*+0.26 ± 0.08*	*78*	*+0.22 ± 0.10*	*9*
2MASS J04443859−0724378	5900	4.4	1.5	+0.03 ± 0.09	64	+0.03 ± 0.08	11
Strip							
2MASS J03494386−1353108	5400	4.5	1.4	+0.00 ± 0.09	64	−0.01 ± 0.12	9
″	*5500*	*4.6*	*1.6*	*+0.05 ± 0.09*	*70*	+0.03 ± 0.13	*10*
2MASS J05274490+0313161	5000	4.3	1.7	−0.02 ± 0.17	51	−0.01 ± 0.23	3
2MASS J06134773+0846022	5050	3.6	1.6	−0.25 ± 0.13	59	−0.24 ± 0.13	9
2MASS J06203205+1331125	5350	4.4	0.3	−0.23 ± 0.17	44	−0.24 ± 0.25	4
2MASS J06350191+1211359	6100	4.3	1.5	+0.01 ± 0.13	45	+0.00 ± 0.19	9
2MASS J06513955+1828080	5100	4.7	1.5	−0.07 ± 0.09	60	−0.07 ± 0.13	5
Alcalá et al. (2000) Sample							
RX J0515.6−0930	5650	4.5	2.3	−0.04 ± 0.12	41	−0.06 ± 0.23	4
RX J0517.9−0708	5100	4.2	1.8	+0.06 ± 0.13	47	+0.05 ± 0.14	4
RX J0531.6−0326	5250	4.3	1.7	−0.02 ± 0.09	53	−0.03 ± 0.08	5
RX J0538.9−0624	5550	4.4	1.3	+0.01 ± 0.11	58	+0.02 ± 0.20	10
RX J0518.3+0829	5300	4.2	2.0	−0.04 ± 0.11	21	−0.02 ± 0.15	3
RX J0510.1−0427	4950	4.6	1.9	−0.10 ± 0.12	34	−0.00 ± 0.24	2
RX J0520.0+0612	4750	4.1	2.2	−0.17 ± 0.12	45	−0.17 ± 0.30	5
RX J0520.5+0616	4900	4.1	2.4	−0.08 ± 0.17	29	−0.07 ± 0.04	3

Notes. The two stars observed with FEROS are indicated in italics. (*) The iron abundances are relative to the Sun. Adopting $T_{\rm eff}^{\odot}$ = 5770 K, $\log g^{\odot}$ = 4.44, and $\xi^{\odot}$ = 1.1 km s^{-1}, we obtain $\log n^{\odot}$(Fe I) = 7.53 ± 0.04 and $\log n^{\odot}$(Fe II) = 7.53 ± 0.06 from a FOCES spectrum, and $\log n^{\odot}$(Fe I) = 7.50 ± 0.05 and $\log n^{\odot}$(Fe II) = 7.50 ± 0.06 from a FEROS spectrum. (**) The listed errors are the internal ones in *EW*, represented by the standard deviation on the mean abundance determined from all lines. The other source of internal error includes uncertainties in stellar parameters (Biazzo et al. 2011a). Taking into account typical errors in $T_{\rm eff}$ (∼70 K), $\log g$ (∼0.2 dex), and ξ (∼0.2 dex), we derive an error of ∼0.05 dex in [Fe/H] due to uncertainties on stellar parameters.

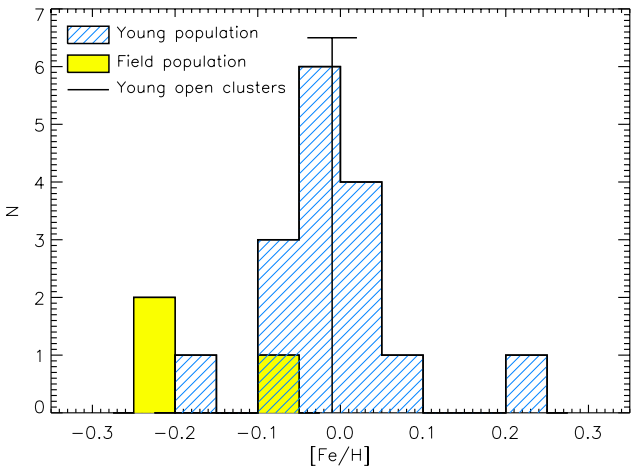

Fig. 8. [Fe/H] distribution for stars observed with the FOCES spectrograph and representing the young population (dashed histogram) and the field population (filled histogram). The bar represents the mean value of [Fe/H] = −0.01 ± 0.03 obtained for open clusters younger than 150 Myr within 500 pc from the Sun (see Biazzo et al. 2011a, and references therein).

inate the young star population detected in soft X-ray survey (Frasca et al. 2006; Guillout et al. 2009). The eight stars with Hα emission, but no Li absorption identified by us (cf. Sect. 4.2) may represent this type of objects.

In Fig. 9, we compare the RASS stellar counterparts (taken from the Guide Star Catalog) in our field with the current X-ray Galactic model predictions using a cumulative distribution function $\log N(>S) - \log S$. We selected two fields: one centered on the Galactic plane ($b_{\rm II}$ = 0° ± 10°, 190° < $l_{\rm II}$ < 220°), and the other, southern, includes Orion and a section of the Gould Belt ($b_{\rm II}$ = −20° ± 10°, 190° < $l_{\rm II}$ < 220°). The deviation from a power-law function for both data distributions at a count rate of ≈0.03 cnts/s is related to the completeness limit of the RASS at this value. Comparing these two distributions, it is noticeable how the source density in the area containing Orion exceeds that of the Galactic plane by about 30−60% (at the highest count rates even by a factor of two). Considering that the population of old active binaries is not yet taken into account in our X-ray model, the predictions closely agree with the RASS data around the Galactic plane and with optical counterparts from the Guide Star Catalog. This model predicts a surface density of 0.37 stars/deg^2 for the Galactic plane at the RASS completeness limit (see Table 3). The source excess in the Orion field can be attributed to additional, probably younger, X-ray active stars generated by recent, more localized star formation that is not included in the Galactic model. In fact, the difference in surface density between the regions in Orion + Gould Belt and the Gould Belt alone is 0.14 ± 0.04 stars/deg^2 for the RASS stellar counterparts and of 0.21 ± 0.07 stars/deg^2 for the stars with lithium detection, i.e. a significant number of young stars in the general direction of Orion is evident that did not necessarily originate in the star formation complex (see Table 3, where the errors were

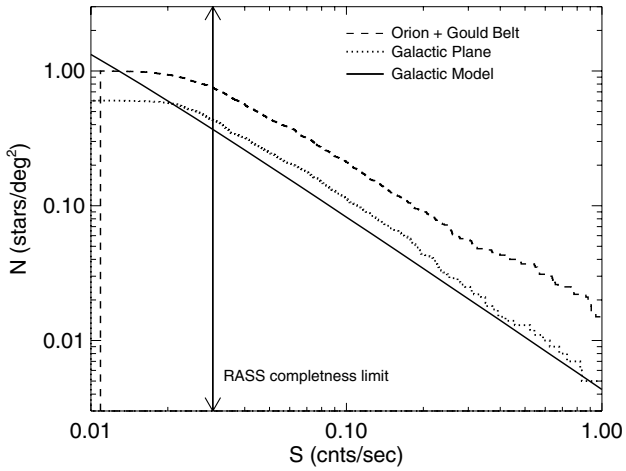

Fig. 9. Cumulative $\log N(>S) - \log S$ distributions for RASS data in the Orion vicinity. A field centered on the Galactic plane is shown with a dotted line. The dashed line includes Orion and a section of the Gould Belt. The solid line corresponds to the prediction of our X-ray models at $l_{II} = 200°$ and zero Galactic latitude. The RASS completeness limit of 0.03 cnts/s is marked with the double arrow.

computed from Poisson statistics). We note that our results are not influenced by the density of active stars: from our spectroscopic identifications, we observed 60 stars in the strip out of 198 young star candidates resulting from the Sterzik et al. (1995) selection criteria. Eight are likely active stars because of their Hα emission but no Li detection (see Sect. 4.2). Therefore, inside the 750 deg^2 strip area, we estimate a surface density of only 0.03 stars/deg^2 as due to active stars.

Encouraged by the success of our X-ray star count modeling in reproducing the background counts and in revealing the excess of sources associated with Orion, we then performed a more detailed analysis of the RASS sources located in the strip shown in Fig. A.1, including the available information on spectroscopic identification and lithium abundance. Our goal is to intercompare average source densities of RASS-selected young stars and to constrain the age distributions in different parts of the strip. Therefore, we divided the strip in three subareas, one is a 200 deg^2 large field centered on the Galactic plane and with $-10° < b_{II} < +10°$, the adjacent 100 deg^2 area between $-20° < b_{II} < -10°$ contains the northern parts of the Orion complex, and the third 100 deg^2 area between $-30° < b_{II} < -20°$ is formally unrelated to the Orion molecular clouds but contains a significant part of the Gould Belt in that direction.

In Fig. 10 we compare the number of RASS sources that have stellar counterparts from the Guide Star Catalog and count rates ≥0.03 cnts/s (as indicated by the thin-lined histogram) with the numbers of these sources predicted by the Galactic model (indicated by star symbols with statistical error bars). The histograms show the X-ray to optical flux ratio distributions. The thick-lined histogram indicates the RASS sources that have been selected as young star candidates according to the Sterzik et al. (1995) criteria. A subsample of those (hatched histogram) were observed spectroscopically and classified according to their lithium absorption strength. The dark gray histogram denotes objects where lithium absorption has been found, and the solid histogram refers to high-lithium stars. We note that the "identified" subsample is by now only complete to 40–70% depending on the area. We can draw the following main conclusions:

1. The total number and the flux ratio distribution of the RASS sources agree well with the Galactic model for the Galactic plane field. High-lithium sources represent about 1/3 of the observed sources. Extrapolating to all RASS-selected young star candidates, we expect a total of about 15 high-lithium sources in this 200 deg^2 large Galactic plane field. The Besançon model predicts 72 X-ray sources with ages younger than 150 Myr in this area. The high-lithium sources are expected to be the youngest within our sample, and we can roughly estimate their characteristic age to be about $15/72 \times 150$ Myr = 30 Myr (assuming continuous star formation). This age is consistent with their spectroscopic signature.
2. A large RASS source excess (~100%) is present in the Orion field. The fraction of high-lithium stars among identified sources is now about 9/10. In this 100 deg^2 field, we expect to find a total of 38 high-lithium stars once all young candidates have been observed.
3. A large RASS source excess (50%) is also present in the field that includes the Gould Belt, preferentially at flux ratios $\log \frac{f_X}{f_V} > -2$. The fraction of high-lithium stars among the observed sources is about 2/3. We expect eventually to find a total of about 17 high-lithium stars in the RASS-selected subsample.

These extrapolations to the total number of expected high-lithium sources should be reliable enough, since the spectroscopic identifications were performed on statistically representative subsamples of RASS-selected young star candidates. It is also possible that some of the high-lithium stars present among RASS sources have been missed by the Sterzik et al. (1995) selection criteria. Hence, the extrapolated number of high-lithium X-ray sources in the respective areas is a lower limit.

The results of this section are summarized in Table 3, where we report the estimated surface density of RASS sources and of high-lithium RASS-selected sources in the three investigated sky areas. While the Galactic plane source densities agree well with the Galactic X-ray star count model, the source density excesses in the other two directions indicate additional populations of high-lithium stars younger than 150 Myr.

5.2. The X-ray clumps 0534+22 and 0430−08: two new young stellar aggregates?

These two groupings were first recognized as surface density enhancements of X-ray emitting young star candidates (see Fig. A.1), and then classified as young star clumps based on the spectroscopic follow-up. In particular, from lithium abundance measurements, the stars in the X-Clump 0534+22 have an age of ~5–10 Myr, while those in the X-Clump 0430−08 of ~2–20 Myr. Inspection of recent CO maps (see Fig. 1) seems to indicate that the stars in the X-Clump 0534+22 follow the spatial location of some of the Taurus-Auriga dark nebulae (namely L1545, L1548, and L1549; Kenyon et al. 2008). Therefore, the X-Clump 0534+22 might be an extension of the Taurus-Auriga association toward the Galactic plane, although the average RV (~22 ± 8 km s^{-1}) of this clump is higher than the mean RV for Taurus, but within the quoted uncertainty. Therefore, it deserves additional kinematic studies. We attempted to estimate the stellar luminosities of the X-Clump 0534+22 stars by assuming the distance to Taurus to be ($d \sim 140$ pc; Kenyon et al. 1994), and adopting the *Tycho* magnitudes (V_{Tycho}; Egret et al. 1992), a solar bolometric magnitude of $M^{\odot}_{bol} = 4.64$ (Cox 2000), and the temperatures listed in Table 4. The resulting HR diagram is shown in Fig. 11. The error in $\log L/L_{\odot}$ is estimated considering an uncertainty of 0.1 mag in V_{Tycho}. The range of ages ~3–30 Myr for

Table 3. Surface densities (in stars/deg^2) of the RASS sources and high-lithium stars compared with the densities as predicted by the X-ray Galactic model for the appropriate Galactic latitude.

	Galactic plane	Orion+Gould Belt	Gould Belt
RASS (>0.03 cnts/s)	0.43 ± 0.02	0.76 ± 0.03	0.62 ± 0.02
Besançon Galactic model	0.37	0.37	0.31
Lithium sources	0.14 ± 0.02	0.39 ± 0.06	0.18 ± 0.04

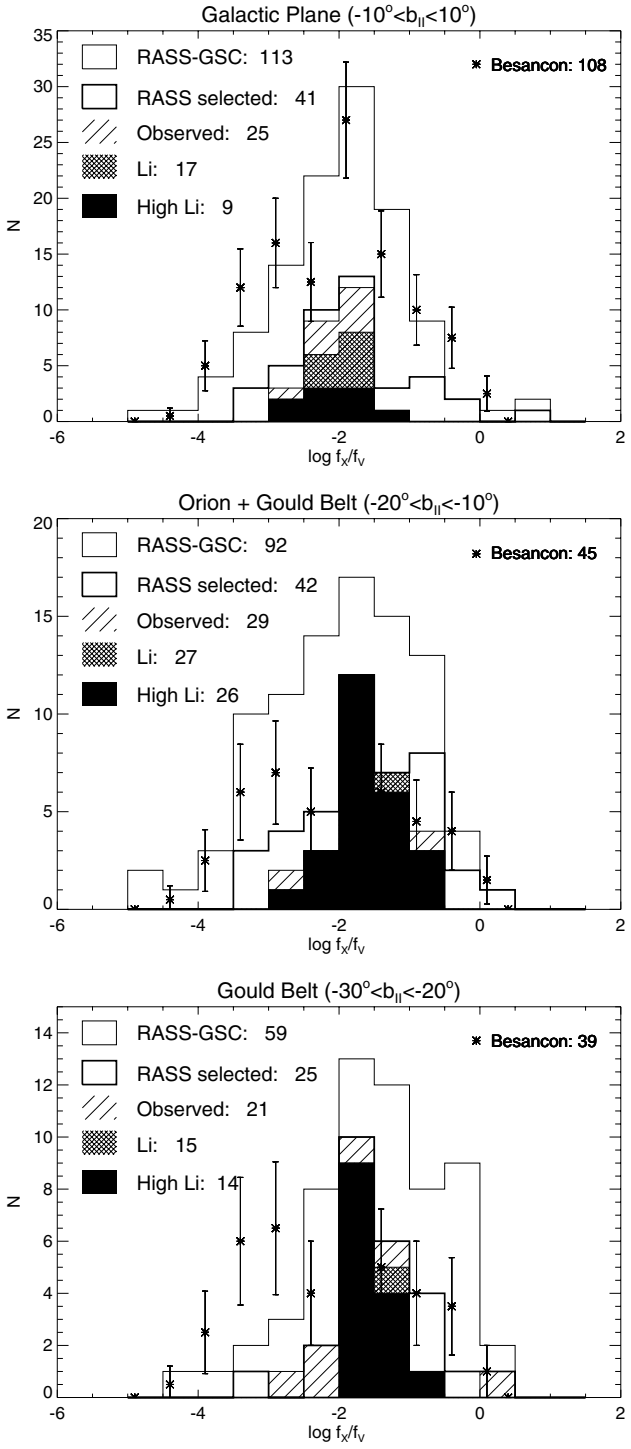

Fig. 10. Detailed comparison of three fields in the strip perpendicular to the Galactic plane between l_{II} = 195° and l_{II} = 205°, as shown in Fig. 2. The three areas include: the Galactic plane, the Orion SFRs, and the Gould Belt, respectively. Histograms are cumulative, not stacked, i.e., each histogram includes the stars in all subcategory histograms.

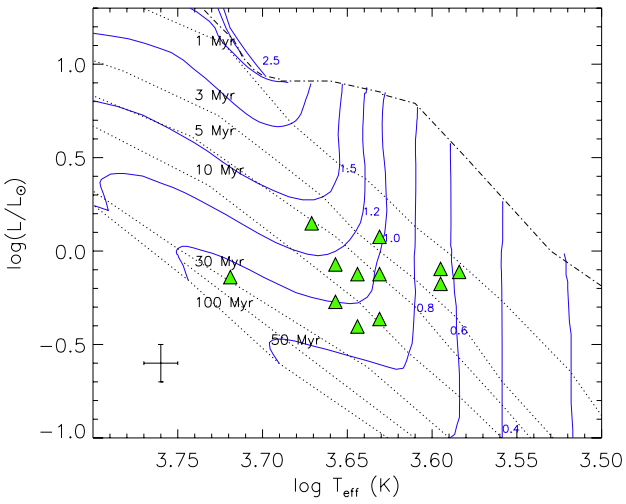

Fig. 11. HR diagram for the stars in the X-Clump 0534+22. The pre-main sequence evolutionary tracks of Palla & Stahler (1999), together with their isochrones and birthline are shown by solid, dotted, and dash-dotted lines, respectively. Labels indicating the track masses and the isochronal ages (from 1 to 100 Myr) are also overlaid.

the stars in the X-Clump 0534+22 appears to be consistent with the estimates from the lithium abundance (see Fig. 5). Adopting instead the Orion distance (~400 pc; Bally 2008) would place the stars close to or above the birthline in the HR diagram, in contrast with their lithium content and lack of IR excess.

5.3. The variety of populations in the Orion vicinity

Based on the morphology and surface density distribution of the X-ray selected young star candidates, the spectroscopic analysis, and the comparison of RASS number counts with Galactic model predictions, we argue that the analyzed widespread stellar sample consists of a mixture of *three distinct populations*:

1. The *clustered population* comprises the dense regions ($\gtrsim$5–10 stars/deg^2) associated with sites of active or recent star formation (e.g., OB1a, OB1b, OB1c, λ Ori, L1616). These clusters contain the highest fraction of lithium-rich stars. The number counts result considerably exceed the Galactic model predictions. The stars in these clusters are, on average, among the youngest in our sample and their low spatial dispersion allows us to locate their birthplace. The RASS limit in X-ray luminosity at $M \sim 0.8\ M_\odot$ is $\sim \log L_X = 30.5$ erg/s; as a consequence, with some caution, we can extrapolate the X-ray luminosity function of RASS sources to lower luminosities (e.g., ~29 erg/s), and estimate the *total number* of X-ray emitting young stars in the Orion complex to be on the order of a few thousand.
2. The broad lane that apparently connects the Orion and Taurus SFRs might contain late-type Gould Belt members

and/or stars belonging to large star halos around Orion and/or Taurus, possibly originated from an earlier episode of star formation. We call this component the *dispersed young population* (density of ∼0.5−5 stars/deg^2). This population appears to be unrelated to any molecular cloud. The number counts in these areas are in significant excess compared to Galactic model expectations. A high fraction of these sources have strong lithium absorption features rather typical of stars with age $\lesssim$20 Myr. They also show an iron abundance distribution consistent with that of nearby open clusters and associations younger than 150 Myr. Recent analysis including parallax information from Hipparcos and *Tycho* suggests that these stars are uniformly distributed along the line of sight, as in the disk-like structure proposed by Guillout et al. (1998) for the GB, and do not pile up at the supposed outer edge of the Gould Belt (Bally 2008). On the other hand, the interpretation of large star halos around Orion and/or Taurus as result of an earlier episode of star formation, e.g. about 20 Myr ago, would require an initial velocity dispersion of nearly 10 km s^{-1} to explain the extension of these halos, whereas the value typically observed for young associations is less than about 2 km s^{-1}, although some authors claim in situ star formation in turbulent cloudlets (Feigelson 1995).

3. The uniformly distributed, *widespread population* has a density $\lesssim$0.5 stars/deg^2 near the Galactic plane and is dominated by stars with a lithium abundance compatible with ZAMS or older ages. The number counts agree with standard Galactic models. However, a few of these stars appear to be of PMS nature, and explaining their origin remains challenging.

Analogous studies based on RASS data and spectroscopic effort are ongoing in the southern hemisphere and within the SACY[10] project (Torres et al. 2006). Preliminary results seem to show two populations: i) an old one associated with evolved stars (similar to what we call the "widespread population"); ii) a young one corresponding to ∼10−100 Myr old associations (e.g., ϵ Cha, Argus, Carina, etc.).

6. Conclusions

We analyzed the young stellar content within the ROSAT X-ray All-Sky Survey on a scale of several thousand square degrees in the general direction of the Orion star-forming region. The study of this young stellar component, through spectroscopic follow-up of a subsample of stars and comparison with Galactic model predictions, leads us to the following conclusions: *The X-ray selected young star candidates consist of a mixture of three distinct populations.*

1. The youngest *clustered population* comprises the dense regions associated with sites of active or recent star formation, where the number counts far exceed the Galactic model predictions.
2. The young *dispersed population* of late-type stars, whose number counts are in significant excess with respect to Galactic model expectations. We cannot firmly establish whether this population represents the late-type component of the Gould Belt or originated from distinct episodes of star formation.
3. The *widespread population* uniformly distributed and dominated by field (ZAMS or older) stars, where the number counts agree with standard Galactic models.

In addition, two new young stellar aggregates, namely the "X-ray clump 0534+22" and the "X-ray clump 0430−08", were singled out. These aggregates deserve future investigation for their complete characterization.

Finally, the future *Gaia*[11] mission will provide trigonometric parallaxes and radial velocities for targets in the general direction of Orion with a precision of a few parsecs at the Orion distance. Knowing the distances to individual stars will permit us to place them on the HR diagram with unprecedented precision, allowing us to firmly establish the origin of the widespread population of young stars on a Galactic scale.

Acknowledgements. This research made use of the SIMBAD database, operated at the CDS (Strasbourg, France). We acknowledge the use of the ESO Science Archive Facility. K.B. acknowledges the financial support from the INAF Postdoctoral fellowship. We thank Fedor Getman for software counsel. We thank the anonymous referee for his/her careful reading and useful comments and suggestions. Last but not least, K.B. gives special thanks to AM-LP-MZ for their moral support during the preparation of the manuscript, and J.M.A. & E.C. are grateful to MD, RNF, and LMS for encouragement to pursue this work.

References

Agresti, A. 1992, Stat. Sci., 7, 131
Alcalá, J. M., Krautter, J., Schmitt, J. H. M. M., et al. 1995, A&A, 114, 109
Alcalá, J. M., Terranegra, L., Wichmann, R., et al. 1996, A&AS, 119, 7
Alcalá, J. M., Chavarria-K., C., & Terranegra, L. 1998, A&A, 330, 1017
Alcalá, J. M., Covino, E., Torres, G., et al. 2000, A&A, 353, 186
Alcalá, J. M., Watcher, S., Covino, E., et al. 2004, A&A, 416, 677
Balachandran, S. C., Mallik, S. V., & Lambert, D. L. 2011, MNRAS, 410, 2526
Bally, J. 2008, in Handbook of Star Forming Regions, Vol. I, ed. B. Reipurth, ASP Conf., 459
Bertout, C., & Genova, F. 2006, A&A, 460, 499
Bessell, M. S., & Brett, J. M. 1988, PASP, 100, 1134
Biazzo, K., Melo, C. H. F., Pasquini, L., et al. 2009, A&A, 508, 1301
Biazzo, K., Randich, S., & Palla, F. 2011a, A&A, 525, A35
Biazzo, K., Randich, S., Palla, F., & Briceño, C. 2011b, A&A, 530, A19
Briceño, C., Hartmann, L., Hernández, J., et al. 2007, A&A, 661, 1119
Broeg, C., Joergens, V., Fernández, M., et al. 2006, A&A, 450, 1135
Covino, E., Melo, C., Alcalá, J. M., et al. 2001, A&A, 375, 130
Cox, A. N. 2000, Allen's Astrophysical Quantities, 4th edn. (New York: AIP Press and Springer-Verlag)
Cutri, R. M., Skrutskie, M. F., van Dyk, S., et al. 2003, Explanatory Supplement to the 2MASS All Sky Data Release
D'Antona, F., & Mazzitelli, I. 1997, MSAIt, 68, 807
Dame, T., Hartmann, D., & Thaddeus, P. 2001, ApJ, 547, 792
Desidera, S., Covino, E., Messina, S., et al. 2011, A&A, 529, A54
Egret, D., Didelon, P., McLean, B. L., Russell, J. L., & Turon, C. 1994, A&A, 258, 217
Elias, F., Alfaro, E. J., & Cabrera-Caño, J. 2009, MNRAS, 397, 2
Favata, F., Sciortino, S., Rosner, R., & Vaiana, G. S. 1988, ApJ, 324, 1010
Favata, F., Barbera, M., Micela, G., & Sciortino, S. 1995, A&A, 295, 147
Feigelson, E. D. 1996, ApJ, 468, 306
Feigelson, E. D., & Montmerle, T. 1999, ARA&A, 37, 363
Frasca, A., Guillout, P., Marilli, E., et al. 2006, A&A, 454, 301
Gandolfi, D., Alcalá, J. M., Leccia, S., et al. 2008, ApJ, 687, 1303
Gontcharov, G. A. 2006, Astron. Lett., 32, 759
Guillout, P., Haywood, M., Motch, C., & Robin, A. C. 1996, A&A, 316, 89
Guillout, P., Sterzik, M. F., Schmitt, J. H. M. M., Motch, C., & Neuhäuser, R. 1998, A&A, 337, 113
Guillout, P., Schmitt, J. H. M. M., Egret, D., et al. 1999, A&A, 351, 1003
Guillout, P., Klutsch, A., Frasca, A., et al. 2009, A&A, 504, 829
Haakonsen, C. B., & Rutledge, R. E. 2009, ApJS, 184, 138
Kaufer, A., Stahl, O., Tubbesing, S., et al. 1999, The Messenger, 95, 8
Kenyon, S. J., & Hartmann, L. 1995, ApJS, 101, 117
Kenyon, S. J., Dobrzycka, D., & Hartmann, L. 1994, ApJ, 108, 1872
Kenyon, S. J., Gómez, M., & Whitney, B. A. 2008, in Handbook of Star Forming Regions, Vol. I, ed. B. Reipurth, ASP Conf., 505
Langsrud, Ø., Jørgensen, K., Ofstad, R., & Næs, T. 2007, J. Appl. Stat., 34, 1275
Lindblad, P. O. 2000, A&A, 363, 154

[10] Search for Associations Containing Young stars.

[11] *Gaia* (Global Astrometric Interferometer for Astrophysics) is an ESA mission that will make the largest, most precise three dimensional map by surveying about one billion stars in our Galaxy and throughout the Local Group.

Marilli, E., Frasca, A., Covino, E., et al. 2007, A&A, 463, 1081
McDowell, J. C. 1994, in Einstein Obs. Unscreened IPC Data Archive
Motch, C., Guillout, P., Haberl, F., et al. 1997, A&A, 318, 111
Palla, F., & Stahler, S. W. 1999, ApJ, 525, 772
Pavlenko, Y. V., & Magazzù, A. 1996, A&A, 311, 961
Pfeiffer, M. J., Frank, C., Baumüller, D., Fuhrmann, K., & Gehren, T. 1998, A&AS, 130, 381
Robin, A., & Crézé, M. 1986, A&A, 157, 71
Sánchez, N., Alfaro, E. J., Elias, F., et al. 2007, ApJ, 667, 213
Santos, N. C., Melo, C., James, D. J., et al. 2008, A&A, 480, 889
Sciortino, S., Favata, F., & Micela, G. 1995, A&A, 296, 370
da Silva, L., Torres, C. A. O., de La Reza, R., et al. 2009, A&A, 508, 833
Sneden, C. 1973, ApJ, 184, 839
Soderblom, D. R., Jones, B. F., & Balachandran, S., et al. 1993, AJ, 106, 1059
Sousa, S. G., Santos, N. C., Israelian, G., Mayor, M., & Monteiro, M. J. P. F. G. 2007, A&A, 469, 783
Sousa, S. G., Alapini, A., Israelian, G., & Santos, N. C. 2010, A&A, 512, A13
Sterzik, M. F., Alcalá, J. M., Neuhäuser, R., & Schmitt, J. H. M. M. 1995, A&A, 297, 418
Szczygieł, D. M., Socrates, A., Paczyński, B., Pojmański, G., & Pilecki, B. 2008, Acta Astron., 58, 405
Torres, G., Neuhäuser, R., & Guenther, E. W. 2002, AJ, 123, 1701
Torres, C. A. O., Quast, G. R., da Silva, L., et al. 2006, A&A, 460, 695
Torres, C. A. O., Quast, G. R., Melo, C. H. F., & Sterzik, M. F. 2008, in Handbook of Star Forming Regions, Vol. II, ed. B. Reipurth, ASP Conf., 757
Voges, W. 1992, in Digitised Optical Sky Surveys, ed. H. T. MacGillivray, & E. B. Thomson (Kluwer Academic Publishers), 453
Voges, W., Aschenbach, B., Boller, Th., et al. 1999, A&A, 349, 389
Walter, F. M., Alcalá, J. M., Neuhäuser, R., Sterzik, M. F., & Wolk, S. J. 2000, in Protostars and Planets IV, ed. V. Mannings, A. P. Boss, & S. S. Russell (University of Arizona Press), 273
Wyse, R. F. G. 2009, in The Age of Stars, ed. E. E. Mamajek, D. R. Soderblom, & R. F. G. Wyse, IAU Symp. 258, 11
Zuckerman, B., & Song., I. 2004, ARA&A, 42, 685

Pages 13 to 16 are available in the electronic edition of the journal at http://www.aanda.org

Table 4. Identified targets with stellar parameters derived through low-resolution and high-resolution spectroscopy.

									LOW RESOLUTION				HIGH RESOLUTION				
Seq	2MASS J	1RXS J	Other name	α (h:m:s)	δ (°:′:″)	J (mag)	H (mag)	K (mag)	Sp.T.	$EW^{\rm hr}_{\rm Li}$ (Å)	$EW_{\rm H\alpha}$ (Å)	$\log T_{\rm eff}$ (K)	$EW^{\rm hr}_{\rm Li}$ (mÅ)	$\log n$(Li) (dex)	$V_{\rm rad}$ (km s^{-1})	$v \sin i$ (km s^{-1})	Note
							Strip										
1	03134743−1701560	050927.0+054145	BD-17 625	03:13:47.439	−17:01:56.09	9.145(0.023)	8.560(0.057)	8.449(0.021)	K0	0	−0.50	3.712	...	...	...	...	
2	03214965−1052179	032149.6−105228	BD-11 648	03:21:49.659	−10:52:17.95	9.837(0.026)	9.380(0.026)	9.264(0.023)	G9	0.250	0.40	3.719	285(10)	3.07	16.1(0.9)	23.4(1.4)	**a**
3	03494386−1353108	034945.1−135315	HD 24091	03:49:43.862	−13:53:10.86	7.553(0.034)	7.185(0.031)	7.070(0.026)	G9	0.150	3.30	3.719	158(5)	2.52	10.9(1.4)	8.3(1.0)	
4	03501928−0726234•	035019.3−072607		03:50:19.281	−07:26:23.49	9.538(0.026)	9.116(0.025)	8.911(0.021)	K0	0.420	0.90	3.712	345(10)	3.29	11.1(1.0)	28.8(1.4)	
5	03503081−1355296•	035030.9−135527	BD-14 758	03:50:30.818	−13:55:29.63	9.061(0.027)	8.626(0.046)	8.440(0.020)	G9	0.220	0.70	3.719	145(10)	2.45	...	...	SB2, **b**, **c**, **d**
6	03563745−1327195•	035637.8−132719		03:56:37.457	−13:27:19.54	9.874(0.023)	9.372(0.022)	9.194(0.019)	K2	0.450	−0.50	3.685	415(10)	3.25	8.5(1.6)	60.1(0.8)	**c**
7	04001941−1200583	040019.2−120026		04:00:19.414	−12:00:58.31	12.152(0.030)	11.670(0.029)	11.571(0.026)	G5	0.180	3.50	3.745	...	...	...	...	
8	04081040−0749034	040810.3−074854	HD 26164	04:08:10.404	−07:49:03.48	7.653(0.021)	7.293(0.033)	7.214(0.023)	G2	0.150	3.05	3.763	...	...	...	...	
9	04150615−0331515	041505.4−033144		04:15:06.151	−03:31:51.52	10.125(0.024)	9.751(0.023)	9.679(0.021)	G9	0.270	1.32	3.719	245(10)	2.89	11.3(1.0)	22.1(1.5)	
10	04231428−0248265	042314.8−024813		04:23:14.287	−02:48:26.54	10.531(0.024)	9.886(0.027)	9.689(0.023)	M0	0	−0.60	3.584	...	...	...	...	
11	04331165−0442029•	043311.6−044200		04:33:11.655	−04:42:02.97	10.983(0.023)	10.396(0.026)	10.239(0.023)	K3	0.570	−0.58	3.671	485(10)	3.36	11.7(0.9)	12.7(2.3)	
12	04344277−0857184	043440.8−085731		04:34:42.771	−08:57:18.42	10.624(0.027)	10.215(0.026)	10.126(0.024)	K1	0.200	1.60	3.698	...	...	...	...	
13	04344238−0857223	043440.8−085731		04:34:42.390	−08:57:22.35	11.652(0.032)	10.971(0.029)	10.840(0.026)	M0	0	−2.22	3.584	...	...	...	...	
14	04382712−0244070•	043825.9−024419		04:38:27.125	−02:44:07.02	10.075(0.024)	9.621(0.024)	9.480(0.021)	K1	0.300	0.50	3.698	264(10)	2.76	23.2(1.0)	24.9(0.7)	
15	04401624−0402238	044016.2−040238		04:40:16.245	−04:02:23.81	10.633(0.024)	10.097(0.023)	9.900(0.021)	K6	0	−0.37	3.631	...	...	...	...	
16	04421860+0117399	044219.2+011741	V1330 Tau	04:42:18.609	+01:17:39.94	9.666(0.024)	9.092(0.024)	8.912(0.019)	K5	0	−0.25	3.644	...	...	...	...	**e**, RS Var.
17	04500470+0150425	045005.7+015101	V1831 Ori	04:50:04.700	+01:50:42.56	10.184(0.022)	9.734(0.024)	9.598(0.023)	G9	0.270	0.48	3.719	290(10)	3.12	24.5(1.3)	66.8(5.7)	SB1, **f**
18	04554346+0205159•	045543.2+020507		04:55:43.465	+02:05:16.00	10.007(0.023)	9.581(0.022)	9.475(0.021)	G6	0.310	1.35	3.738	315(10)	3.41	12.6(1.5)	21.7(2.0)	
19	05045754−0354527	050457.8−035451	HD 32704	05:04:57.545	−03:54:52.75	6.865(0.024)	6.378(0.023)	6.259(0.020)	G9	0.070	1.00	3.719	...	...	...	...	
20	05055785+0323326	050558.2+032331		05:05:57.857	+03:23:32.67	10.903(0.026)	10.489(0.028)	10.359(0.025)	G9	0.300	1.35	3.719	235(10)	2.89	16.8(1.5)	19.3(2.0)	
21	05091558+0343483	050915.7+034339		05:09:15.589	+03:43:48.33	11.112(0.023)	10.499(0.023)	10.335(0.019)	K7	0.550	−1.55	3.618	475(10)	2.52	17.2(1.5)	25.0(2.0)	
22	05103912+0554261•	051038.6+055432		05:10:39.129	+05:54:26.15	10.254(0.022)	9.654(0.029)	9.485(0.021)	M0*	...	−0.35*	3.584*	435(5)	1.93	21.4(1.4)	22.2(2.0)	
23	05113738+0255163•	051136.5+025457		05:11:37.381	+02:55:16.36	12.675(0.026)	12.395(0.024)	12.298(0.027)	F8	0.180	5.10	3.796	...	...	...	...	
24	05133474+0554377•	051334.2+055449		05:13:34.744	+05:54:37.77	9.733(0.024)	9.343(0.024)	9.224(0.022)	G8	0.360	1.15	3.725	295(5)	3.19	17.8(2.0)	38.8(2.0)	
25	05274490+0313161	052744.2+031329		05:27:44.901	+03:13:16.15	13.610(0.027)	12.955(0.031)	12.896(0.034)	K0	0.380	−0.05	3.712	412(5)	3.55	10.9(1.4)	14.3(1.5)	
26	05281274−0131248	052744.2+031329		05:28:12.744	−01:31:24.87	10.806(0.023)	10.555(0.022)	10.490(0.025)	F8	0.150	3.45	3.796	...	...	...	...	
27	05281224−0131156	052819.1−013011		05:28:12.250	−01:31:15.61	11.558(0.024)	11.157(0.022)	11.092(0.025)	G0	0.340	1.45	3.774	...	...	...	...	
28	05303519+0220423	053035.9+022050		05:30:35.197	+02:20:42.33	10.577(0.022)	10.177(0.021)	10.063(0.021)	K0	0.420	1.60	3.712	335(10)	3.22	20.3(1.4)	20.7(2.0)	
29	05384831+0923557	053847.7+092407		05:38:48.319	+09:23:55.80	10.482(0.024)	10.138(0.022)	10.016(0.019)	G8	0.230	1.95	3.725	...	...	...	...	
30	05445517+1035142	054454.3+103513		05:44:55.179	+10:35:14.26	10.233(0.022)	9.843(0.027)	9.715(0.023)	K0	0.210	1.05	3.712	...	...	...	...	
31	05445274+1035173	054454.3+103513		05:44:52.740	+10:35:17.35	12.155(0.022)	11.906(0.024)	11.754(0.025)	F9	0.160	5.40	3.785	...	...	...	...	
32	05540858+1219358	055408.6+121924	HD 248994	05:54:08.581	+12:19:35.89	8.954(0.018)	8.671(0.034)	8.550(0.016)	G0	0.160	2.45	3.774	146(10)	3.06	38.0(1.4)	16.2(1.5)	
33	06030836+0352208	060308.6+035218		06:03:08.370	+03:52:20.86	11.256(0.024)	10.855(0.022)	10.729(0.019)	K5	0.340	0.50	3.644	350(10)	2.37	27.6(4.2)	58.8(2.0)	SB?
34	06030764+0352112	060308.6+035218		06:03:07.650	+03:52:11.24	11.775(0.024)	11.277(0.022)	11.129(0.021)	G9	0.320	1.40	3.719	...	...	...	...	
35	06043473+0508489•	060434.3+050902		06:04:34.732	+05:08:48.91	9.917(0.022)	9.536(0.028)	9.461(0.021)	G8	0.270	1.80	3.725	230(5)	2.90	17.5(1.4)	21.5(2.0)	
36	06055511+1228499	060555.7+122842		06:05:55.112	+12:28:49.92	10.138(0.020)	9.462(0.023)	9.259(0.019)	M1	0	−2.90	3.564	...	...	...	...	
37	06124499+0944227•	061244.8+094422		06:12:44.995	+09:44:22.71	8.579(0.026)	7.997(0.027)	7.813(0.029)	K0	0	0.28	3.712	...	...	...	...	
38	06134815+0846160•	061347.5+084617		06:13:48.153	+08:46:16.01	9.536(0.024)	9.011(0.023)	8.891(0.021)	K2	0.420	0.75	3.685	335(10)	2.86	35.7(2.0)	61.6(2.0)	
39	06134773+0846022	061347.5+084617		06:13:47.738	+08:46:02.25	9.555(0.024)	9.022(0.023)	8.915(0.023)	K1	0.270	−0.89	3.698	...	...	16.4(1.3)	5.4(0.5)	
40	06154049+1315332	061540.0+131537	HD 254104	06:15:40.490	+13:15:33.30	9.630(0.018)	9.492(0.021)	9.413(0.017)	F3	0.090	5.50	3.840	...	...	...	...	
41	06153978+1315421	061540.0+131537		06:15:39.787	+13:15:42.20	11.160(0.019)	10.752(0.021)	10.669(0.018)	G9	0.240	1.65	3.719	...	...	...	...	
42	06203205+1331125•	062031.8+133107	HD 255438	06:20:32.057	+13:31:12.58	8.178(0.027)	7.921(0.017)	7.854(0.016)	...	...	...	...	0	...	21.9(0.9)	9.6(0.5)	
43	06261917+1214546	062617.3+121510		06:26:19.178	+12:14:54.61	10.170(0.020)	10.015(0.020)	9.971(0.017)	F1	0.050	6.00	3.856	...	...	...	...	
44	06261740+1215180	062617.3+121510		06:26:17.406	+12:15:18.06	10.978(0.021)	10.404(0.023)	10.223(0.018)	K6	0.370	−3.10	3.631	300(30)	...	18.0(2.3)	89.5(1.6)	
45	06300125+1625225	063000.9+162524		06:30:01.255	+16:25:22.52	9.168(0.022)	8.715(0.021)	8.539(0.017)	...	...	...	...	0	...	22.7(1.5)	55.4(1.5)	
46	06350191+1211359	‡		06:35:01.911	+12:11:35.93	10.408(0.024)	10.168(0.025)	10.101(0.018)	...	...	...	...	80(10)	...	37.9(0.8)	6.7(0.1)	
47	06382516+1240517	‡		06:38:25.169	+12:40:51.76	10.297(0.023)	9.638(0.022)	9.443(0.018)	K6	0	−0.90	3.631	...	...	...	...	
48	06413601+0802055•	064136.2+080218	HD 262113	06:41:36.010	+08:02:05.54	9.263(0.026)	8.781(0.051)	8.712(0.023)	K1*	0.160	1.40	3.698*	160(15)	2.28	19.9(1.4)	45.1(2.0)	SB2?, **g**
49	06453046+1507432	064529.9+150757		06:45:30.462	+15:07:43.29	10.878(0.022)	10.419(0.028)	10.251(0.021)	...	...	...	...	0	...	58.7(2.7)	>100.0	SB?
50	06471556+1434392•	064715.8+143435		06:47:15.568	+14:34:39.27	8.850(0.020)	8.302(0.029)	8.133(0.026)	K1	0.100	0.25	3.698	...	...	...	...	
51	06513955+1828080◇	065140.3+182801	TYC 1335-648-1	06:51:39.551	+18:28:08.08	7.886(0.021)	7.395(0.027)	7.291(0.020)	...	...	...	...	0	...	−7.4(0.9)	7.5(0.7)	

Table 4. continued.

Seq	2MASS J	1RXS J	Other name	α (h:m:s)	δ (mag)	J (mag)	H (mag)	K (°:′:″)	LOW RESOLUTION Sp.T.	$EW_{\rm Li}^{\rm lr}$ (Å)	$EW_{\rm H\alpha}$ (Å)	$\log T_{\rm eff}$ (K)	HIGH RESOLUTION $EW_{\rm Li}^{\rm hr}$ (mÅ)	$\log n$(Li) (dex)	$V_{\rm rad}$ (km s^{-1})	$v \sin i$ (km s^{-1})	Note
52	06515913+0936218•	065158.8+093630		06:51:59.137	+09:36:21.87	9.491(0.021)	8.978(0.024)	8.858(0.023)	G8	0.350	−1.80	3.725	350(10)	3.45	24.3(0.9)	22.3(1.1)	
53	06545126+1611078	065450.7+161112		06:54:51.267	+16:11:07.87	9.854(0.022)	9.311(0.028)	9.236(0.020)	...	...	...	...	80(10)	...	−5.0(0.8)	32.5(0.5)	
54	06550482+2018560•	065505.3+201855	HD 266141	06:55:04.825	+20:18:56.03	8.412(0.021)	8.192(0.017)	8.134(0.024)	...	...	...	...	55(10)	...	−12.0(1.5)	59.6(1.6)	
55	07002586+1643084	070026.0+164325		07:00:25.866	+16:43:08.45	9.586(0.029)	9.107(0.030)	8.962(0.022)	K3*	...	1.20*	3.671*	165(10)	1.98	91.7(0.9)	26.3(1.4)	
56	07011843+1528366	070118.7+152849		07:01:18.439	+15:28:36.61	10.729(0.024)	10.138(0.030)	10.038(0.019)	K1	0	−0.55	3.698	...	...	...	...	
57	07023741+1558261•	070237.1+155843	HD 52634	07:02:37.414	+15:58:26.17	7.158(0.023)	6.918(0.038)	6.873(0.020)	F9	0.170	3.28	3.785	150(10)	3.17	25.8(1.4)	22.2(2.0)	**h**, Doub. Syst.
58	07071097+2011394	070710.2+201136	TYC 1353-331-1	07:07:10.974	+20:11:39.41	9.289(0.024)	9.003(0.024)	8.958(0.018)	F9	0.060	3.90	3.785	...	...	...	...	
59	07110918+1312442	071109.2+131246		07:11:09.183	+13:12:44.24	8.644(0.027)	8.014(0.018)	7.848(0.023)	M2	0	0.18	3.547	...	...	...	...	
60	07181093+1735160•	071811.4+173515		07:18:10.930	+17:35:16.01	8.592(0.026)	8.111(0.018)	7.978(0.027)	K0	0.300	1.20	3.712	350(30)	3.29	...	...	
							X-Clump 0534+22										
61	05203710+2447135•	052036.6+244731	V1360 Tau	05:20:37.104	+24:47:13.54	9.767(0.020)	9.257(0.022)	9.072(0.017)	K5	0.370	~0.0	3.644	435(10)	2.73	20.7(1.2)	103.3(11.3)	RS Var.
62	05214684+2400444•	052146.7+240036	V1361 Tau	05:21:46.844	+24:00:44.43	8.592(0.026)	8.111(0.018)	7.978(0.027)	K3	0.350	−0.40	3.671	395(5)	2.93	14.2(1.4)	15.6(1.0)	**i**, T Tau
63	05221036+2432089•	052210.2+243200	V1362 Tau	05:22:10.360	+24:32:08.96	8.556(0.023)	7.991(0.018)	7.889⋆	G9	0.330	−0.25	3.719	365(10)	3.45	19.1(1.4)	26.8(2.0)	RS Var.
64	05224717+2437311•	052248.0+243731	V1363 Tau	05:22:47.171	+24:37:31.13	9.268(0.024)	8.670(0.031)	8.480(0.023)	K4	0.490	−0.20	3.657	475(10)	3.08	21.4(1.9)	46.4(2.0)	RS Var.
65	05263833+2231546•	052638.7+223151		05:26:38.334	+22:31:54.66	10.119(0.022)	9.536(0.022)	9.415(0.020)	K5	0.280	−0.04	3.644	290(5)	2.15	28.0(1.4)	14.4(1.0)	T Tau
66	05263826+2231434•	052638.7+223151		05:26:38.269	+22:31:43.48	10.001(0.021)	9.478(0.022)	9.340(0.017)	K6	0.290	−0.14	3.631	285(10)	1.91	28.3(1.4)	10.0(1.0)	T Tau
67	05270306+2041508	052703.5+204204		05:27:03.066	+20:41:50.86	9.255(0.021)	8.542(0.026)	8.410(0.017)	K7-M0	0.400	−1.20	3.595	447(10)	2.12	12.8(1.4)	12.7(1.0)	
68	05271996+2503434	052720.0+250348		05:27:19.962	+25:03:43.46	10.445(0.023)	9.757(0.022)	9.547(0.018)	M0	0.430	−1.50	3.584	515(10)	2.24	17.5(1.4)	11.3(1.0)	
69	05322227+2521077◇	053222.9+252106	TYC 1852-1665-1	05:32:22.279	+25:21:07.77	9.029(0.021)	8.683(0.022)	8.603(0.019)	G7	0	2.23	3.732	...	...	...	...	
70	05332381+2019575•	053323.5+201951	TYC 1305-353-1	05:33:23.816	+20:19:57.50	8.789(0.023)	8.328(0.024)	8.270(0.020)	K0	0	1.55	3.712	...	...	...	...	
71	05394828+2614008	053948.9+261427		05:39:48.287	+26:14:00.84	10.054(0.020)	9.678(0.022)	9.561(0.017)	...	...	...	...	30(10)	...	34.5(2.2)	19.3(1.0)	
72	05410142+2036179•	054101.8+203624		05:41:01.429	+20:36:17.96	9.160(0.021)	8.659(0.021)	8.504(0.018)	K6	0.300	−1.20	3.631	375(10)	2.31	34.5(1.2)	76.9(4.7)	
73	05463252+2435382	054632.7+243549		05:46:32.524	+24:35:38.25	9.651(0.021)	9.200(0.021)	9.068(0.017)	K4	0.300	0.90	3.657	380(5)	2.67	19.9(1.4)	24.2(2.0)	
74	05463283+2240315	054632.8+224041		05:46:32.831	+22:40:31.54	9.685(0.021)	9.031(0.024)	8.896(0.020)	K6	0.400	−0.20	3.631	315(10)	2.03	15.4(1.4)	12.8(1.0)	
75	06020094+1955290	‡		06:02:00.942	+19:55:29.02	11.269(0.023)	10.705(0.032)	10.546(0.020)	K7-M0	0.170	−0.75	3.595	130(10)	0.77	13.4(1.3)	22.9(0.1)	
							L1616 Clump										
76	04591458−0337062◇	045912.4−033711		04:59:14.023	−03:37:06.08	10.070(0.022)	9.616(0.024)	9.474(0.020)	G7	0.340	0.35	3.732	355(10)	3.53	12.2(1.6)	32.4(2.0)	**g**, **m**, **n**, T Tau
77	05041593−0214505◇	050416.9−021426		05:04:15.932	−02:14:50.51	10.661(0.024)	10.105(0.024)	9.984(0.025)	K3	0.490	−0.18	3.671	475(10)	3.30	19.8(1.5)	29.1(2.0)	**m**, **n**, T Tau
78	05090066−0315066•	050859.6−031503	V1849 Ori	05:09:00.662	−03:15:06.63	9.914(0.024)	9.530(0.024)	9.408(0.021)	K1*	...	1.29*	3.698*	320(10)	2.99	23.4(2.0)	40.6(2.0)	**c**, **l**, **m**, **n**, T Tau
79	05101086−0254049◇	051011.5−025355	V1011 Ori	05:10:10.860	−02:54:04.94	10.454(0.022)	9.952(0.024)	9.730(0.023)	K1	0.480	0.35	3.698	415(10)	3.45	26.1(1.5)	31.2(2.0)	**m**, **n**, T Tau
80	05101478−0330074	051015.7−033001		05:10:14.783	−03:30:07.40	10.038⋆	9.806(0.060)	9.749(0.049)	G9*	...	1.10*	3.719*	320(10)	3.24	19.0(1.8)	34.6(2.0)	**l**, **m**, **n**, T Tau
81	05104050−0316415	051043.2−031627	TYC 4755-873-1	05:10:40.504	−03:16:41.56	10.079(0.026)	9.735(0.022)	9.648(0.025)	G5	0.240	2.70	3.745	235(10)	3.20	20.1(2.6)	78.9(2.0)	**m**, **n**, T Tau
82	05122053−0255523	051219.9−025547	V531 Ori	05:12:20.531	−02:55:52.34	10.425(0.023)	9.688(0.023)	9.140(0.019)	K3*	...	−6.35*	3.671*	395(10)	2.93	23.3(1.2)	34.0(1.8)	**l**, **m**, **n**, Var. Rapid
							X-Clump 0430−08										
83	04405981−0840023	044059.2−084005	MM Eri	04:40:59.812	−08:40:02.38	8.880(0.023)	8.528(0.026)	8.558(0.027)	G7*	...	2.50*	3.732*	168(10)	2.69	20.8(1.5)	29.9(2.0)	**b**, **c**, RS Var.
84	04354055−1017293•	043541.2−101731	TYC 5317-3258-1	04:35:40.553	−10:17:29.36	9.620(0.024)	9.269(0.024)	9.174(0.023)	K1*	...	3.50*	3.698*	195(10)	2.47	14.5(1.8)	34.0(2.0)	
85	04431640−0937052	2E 0440.9−0942△	HD 29980	04:43:16.408	−09:37:05.28	6.971(0.021)	6.693(0.055)	6.621(0.023)	G5*	...	3.40*	3.745*	85(5)	2.45	33.5(0.9)	5.7(0.1)	**h**, Doub. Syst.
86	04463244−0857241	044632.7−085723	TYC 5322-1381-1	04:46:32.450	−08:57:24.20	9.142(0.032)	8.466(0.026)	8.393(0.024)	K2*	...	1.40*	3.685*	0	...	−10.9(1.3)	22.0(2.0)	
87	04503013−0837103	045029.9−083701		04:50:30.137	−08:37:10.39	10.581(0.024)	10.048(0.024)	9.900(0.021)	K4*	...	0.27*	3.732*	210(10)	2.92	16.0(0.9)	15.0(0.4)	
88	04443859−0724378	044437.9−072439	BD-07 888	04:44:38.595	−07:24:37.87	8.332(0.024)	8.033(0.046)	7.968(0.021)	G7*	0.200	3.30*	3.732*	160(5)	2.66	23.1(0.9)	3.4(0.1)	
89	04383054−0645583•	043830.8−064559	TYC 4747-376-1	04:38:30.548	−06:45:58.36	9.608(0.029)	9.274(0.026)	9.132(0.026)	G0	0.210	2.55	3.774	210(10)	3.37	3.8(1.5)	22.5(2.0)	
90	04390790−0805581	043905.9−080619		04:39:07.902	−08:05:58.11	10.202(0.027)	9.747(0.022)	9.614(0.021)	G9	0.410	1.10	3.719	350(10)	3.38	14.7(1.7)	36.4(2.0)	

Notes. (*) Values obtained from high-resolution spectra. (‡) Star not present in the ROSAT All-Sky Bright Source Catalog. (△) Designation of the *Einstein* Soft X-ray Source List (McDowell 1994). (⋆) 2MASS magnitude of low quality. (•) Already identified as 2MASS point source by Haakonsen & Rutledge (2009). (◇) Already identified as 2MASS point source by *SIMBAD*.
SB1: single-lined spectroscopic binary; SB2: double-lined spectroscopic binary; SB2?: suspected spectroscopic binary; SB?: suspected spectroscopic multiple. *SIMBAD* notes: Susp. Var.: Star suspected of variability; RS Var.: Variable of RS CVn type; Doub. Syst.: Star in double system; T Tau: T Tau-type star; Var. Rapid: Variable star with rapid variations.

References. Main references: **a)** da Silva et al. (2009); **b)** Covino et al. (2001); **c)** Marilli et al. (2007); **d)** Favata et al. (1995); **e)** Torres et al. (2002); **f)** Broeg et al. (2006); **g)** Szczygieł et al. (2008); **h)** Gontcharov (2006); **l)** Alcalá et al. (2000); **m)** Alcalá et al. (2004); **n)** Gandolfi et al. (2008).

Appendix A: Large-scale spatial distribution of the targets

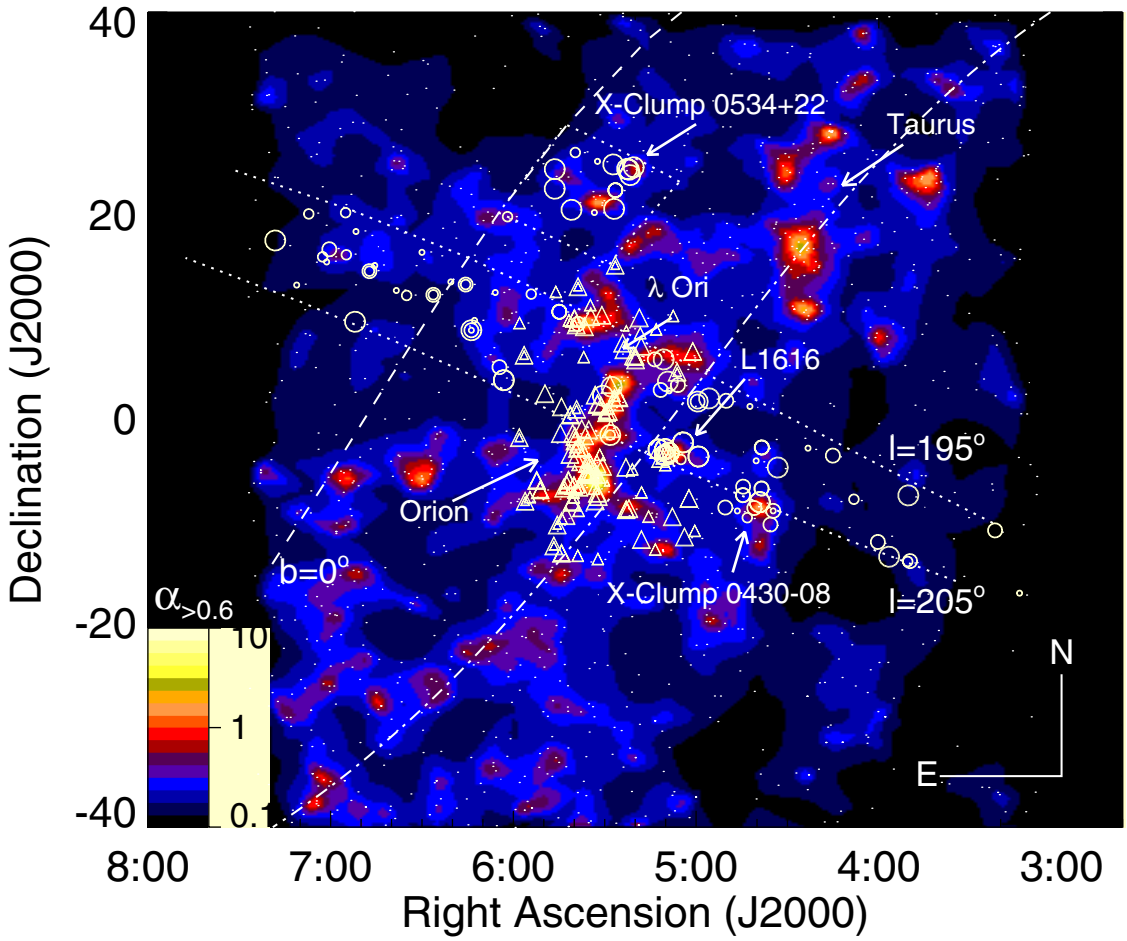

Fig. A.1. Large-scale spatial distribution of 1483 candidate young stars (small dots) in the Orion and Taurus-Auriga associations. The X-ray sources have been selected from the ROSAT All-Sky Survey. Their space density is color-coded, where the parameter α represents the discriminant probability; the higher α, the more probable is the occurrence of a source corresponding to a young star. Circles refer to sources observed spectroscopically in this work, while triangles represent targets previously analyzed by Alcalá et al. (1996) and Alcalá et al. (2000). The symbol size increases with the lithium equivalent width *EW* (0, <150, 150–300, >300 mÅ). The dashed line coincides with the position of the Galactic plane, while the dash-dotted line represents the Gould Belt, as given by Guillout et al. (1998). The sky strip ($195° < l_{II} < 205°$, $-60° < b_{II} < 15°$) selected by us across the Gould Belt in the Orion vicinity is also shown together with the area selected on the X-Clump 0534+22 (see Sect. 4). The regions of enhanced density of young star candidates and of high-lithium stars southward of the Galactic plane coincide with the location of the Gould Belt midplane. North is up and East to the left.

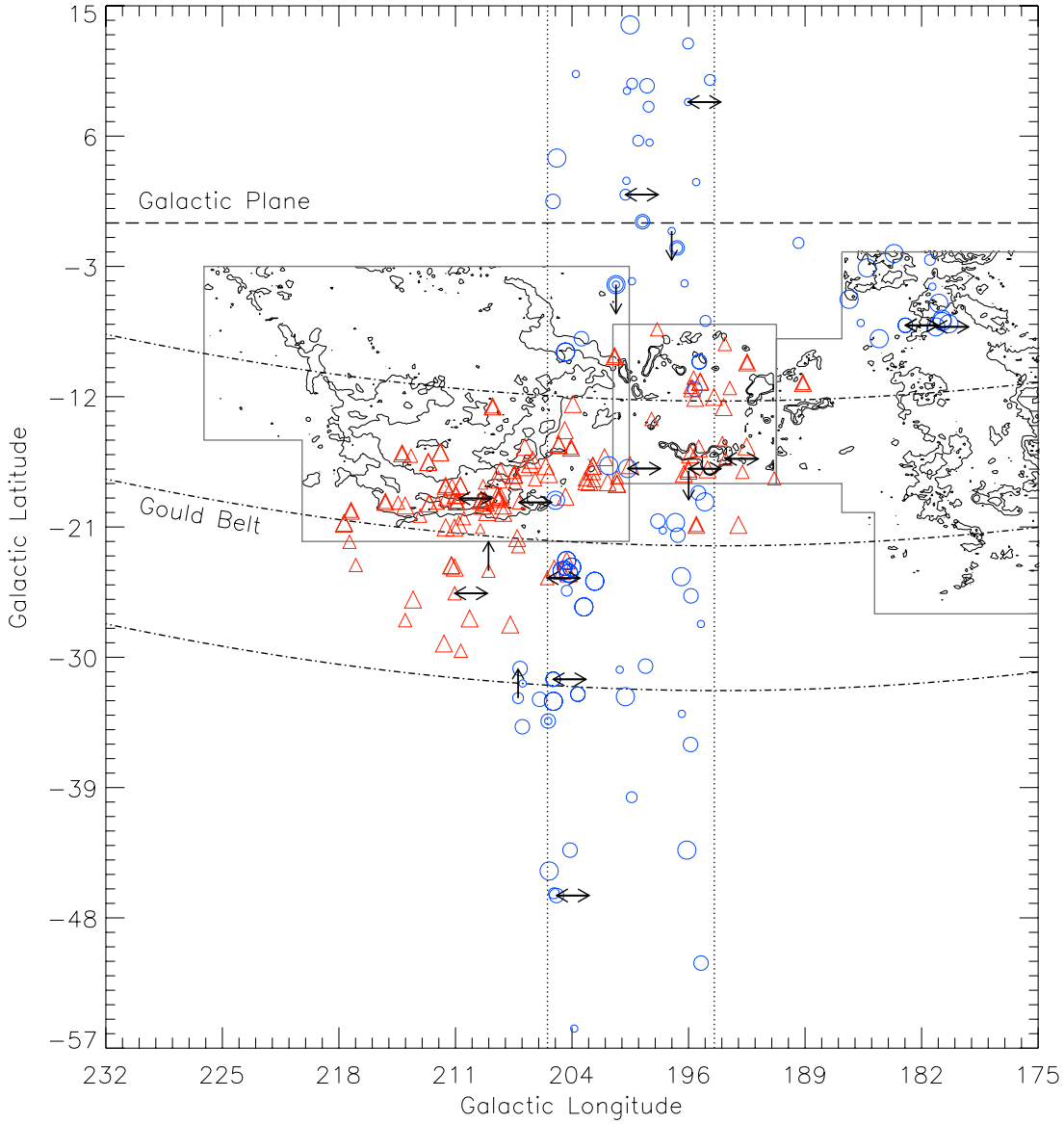

Fig. A.2. Large-scale spatial distribution of all targets observed at low and/or high resolution. Circles refer to sources observed spectroscopically in this work, while triangles are targets analyzed by Alcalá et al. (1996) and Alcalá et al. (2000). The symbol size increases with the lithium equivalent width (0, <150, 150–300, >300 mÅ). The arrows refer to stars for which we measured the iron abundance (downward for [Fe/H] ≤ -0.14, horizontal for $-0.14 <$ [Fe/H] ≤ 0.06, upward for [Fe/H] > 0.06; the central bin corresponds to the average metallicity of our targets $\pm 1\sigma$). Dotted lines represent the strip, long-dashed line is the Galactic plane, while dash-dotted lines represent the Gould Belt disk, as outlined by Guillout et al. (1998). The CO $J = 1 \rightarrow 0$ emission contour maps by Dame et al. (2001) of the Orion, Monoceros, and Taurus molecular clouds, and the λ Orionis H II region are also overlaid.